

ARTICLE

A mechanism for pathological oscillations in mouse retinal ganglion cells in a model of night blindness

Sho Horie¹ , Konan Sakuta¹ , Keigo Tada² , Haruki Tokumoto¹ , Taketo Nishimoto¹ , Katsunori Kitano^{3,4,5} , Masao Tachibana⁴ , and Chieko Koike^{4,5,6} 

TRPM1 channels, regulated by mGluR6 at the dendrites of retinal ON bipolar cells (BCs), play a crucial role in visual signal transduction. Both *Trpm1* knockout (KO) and *mGluR6* KO mice are models of congenital stationary night blindness with grossly normal morphology. However, robust pathological spontaneous oscillations in retinal ganglion cells (RGCs) have been observed in *Trpm1* KO retinas but not in *mGluR6* KO retinas. We investigated the mechanism underlying these oscillations in the *Trpm1* KO retina using whole-cell clamp techniques. We found that inhibitory and excitatory synaptic inputs produced anti-phase oscillations in OFF and ON RGCs, respectively, and that oscillations could be suppressed by blockers targeting the All amacrine cell (AC) pathway. The *rd1* retina, a model for retinitis pigmentosa with severe photoreceptor degeneration, displays similar oscillations to the *Trpm1* KO retina. Morphological and immunohistochemical analyses revealed similar alterations in the *Trpm1* KO and *rd1* retinas when compared to the *mGluR6* KO and wild-type retinas: namely, rod BCs (RBCs) in both *Trpm1* KO and *rd1* retinas showed reduced dendritic TRPM1 labeling and smaller axon terminals. Furthermore, RBCs in the *Trpm1* KO retina were significantly hyperpolarized. *In silico* simulation of the BC-All AC-RGC network suggests that the reduction of RBC and ON cone BC outputs to All ACs contributes to RGC oscillations. Our findings suggest that TRPM1 deficiency in ON BCs produces RGC oscillations in association with RBC axon remodeling and reduced ON BC outputs, and may represent a shared circuit mechanism underlying pathological oscillations across different causes of outer retinal diseases.

Introduction

Retinitis pigmentosa (RP), an inherited disorder characterized by progressive degeneration of photoreceptors, has been studied using model mice with retinal degeneration (*rd*) (Grover et al., 1999; Hartong et al., 2006; Margolis et al., 2008; Goo et al., 2011). In the case of *rd1* mouse, rods are almost completely lost by P30–P40 (Carter-Dawson et al., 1978; Jiménez et al., 1996). Retinal ganglion cells (RGCs) of *rd* mice show pathological oscillatory spontaneous firing (Margolis et al., 2008, 2014; Stasheff, 2008; Borowska et al., 2011; Menzler and Zeck, 2011; Yee et al., 2012; Choi et al., 2014; Poria and Dhingra, 2015). The oscillations in postsynaptic RGCs are driven by oscillations in presynaptic All amacrine cells (ACs) (Borowska et al., 2011; Trenholm et al., 2012; Choi et al., 2014; Margolis et al., 2014). RGC oscillations, often referred to as “noise,” may disrupt visual information processing. Thus, understanding the mechanisms underlying RGC oscillations is crucial for finding effective therapeutic strategies for RP.

It is widely assumed that RGC oscillations in the *rd1* mouse retina may be caused primarily by photoreceptor degeneration,

and that the following All AC oscillations may be induced by intrinsic membrane properties of All ACs (Choi et al., 2014) or by network properties of All ACs and ON cone bipolar cells (ON CBCs) (Trenholm et al., 2012). In addition to RGC oscillations, the *rd1* mouse retina undergoes significant anatomical remodeling. The sprouting neurites from cones develop ectopic synapses with rod bipolar cell (RBC) soma (Haq et al., 2014). Horizontal cells also extend abnormal processes toward the inner plexiform layer (IPL), whereas the dendrites of ON BCs retract (Strettoi and Pignatelli, 2000; Strettoi et al., 2002, 2003; Chen et al., 2012). Various forms of anatomical remodeling hinder our understanding of how photoreceptor degeneration leads to oscillations in the inner retina of the *rd* mice.

In the present study, we focus on the *Trpm1* knockout (KO) mouse, a model for congenital stationary night blindness (CSNB). TRPM1, a member of the transient receptor potential cation channel subfamily M, is a critical visual transduction channel regulated by mGluR6 on the dendrites of ON BCs. Both *Trpm1* KO and *mGluR6* KO mice serve as models of CSNB and

¹Graduate School of Pharmacy, Ritsumeikan University, Kusatsu, Japan; ²Graduate School of Information Science and Engineering, Ritsumeikan University, Ibaraki, Japan; ³College of Information Science and Engineering, Ritsumeikan University, Ibaraki, Japan; ⁴Center for Systems Vision Science, Research Organization of Science and Technology, Ritsumeikan University, Kusatsu, Japan; ⁵Ritsumeikan Global Innovation Research Organization (R-GIRO), Ritsumeikan University, Kusatsu, Japan; ⁶College of Pharmaceutical Sciences, Ritsumeikan University, Kusatsu, Japan.

Correspondence to Chieko Koike: koike@fc.ritsumei.ac.jp; Masao Tachibana: mstchbn@fc.ritsumei.ac.jp; Katsunori Kitano: kkt23219@is.ritsumei.ac.jp.

© 2025 Horie et al. This article is available under a Creative Commons License (Attribution 4.0 International, as described at <https://creativecommons.org/licenses/by/4.0/>).

exhibit a loss of ON responses despite grossly normal retinal structures (Masu et al., 1995; Koike et al., 2009; Morgans et al., 2009; Koike et al., 2010; Nakamura et al., 2010; Xu et al., 2012). However, a notable difference is that pathological spontaneous RGC oscillations are prominently observed in the *Trpm1* KO mouse, whereas oscillations are infrequent or absent in the *mGluR6* KO mouse (Takeuchi et al., 2018; Hasan et al., 2020). Oscillatory activity occurs in other CSNB models, such as *Nyx^{nob}*, *Lrit3^{mrgagl}*, and *Cav1.4* KO mice (Hasan et al., 2020; Hölzel et al., 2023). Notably, disruption of these genes leads to impaired membrane localization of TRPM1 (Pearring et al., 2011; Neuillé et al., 2015; Maddox et al., 2020). In particular, *Nyx* and *Lrit3* play crucial roles in ensuring proper membrane targeting of TRPM1 (Pearring et al., 2011; Neuillé et al., 2015). Taken together, these consistent associations raise the possibility that TRPM1 loss is a key contributing factor in generating oscillatory activity in CSNB—a hypothesis we investigate using *Trpm1* KO mouse retinas.

In this study, we used whole-cell recordings, morphological and immunohistochemical analyses, and computational modeling to investigate the mechanisms underlying RGC oscillations in the *Trpm1* KO mouse retina. We compared *Trpm1* KO and *rdl* mouse retinas and observed shared morphological alterations in RBCs. Using *in silico* models, we examined how TRPM1 loss and these morphological alterations might together contribute to the emergence of oscillatory activity.

Materials and methods

Animals

All animal experimental protocols were approved by the Animal Research Committee of Ritsumeikan University and conducted in accordance with local guidelines and the ARVO Statement for the Use of Animals in Ophthalmic and Vision Research. For electrophysiological experiments, 1- to 2-mo-old wild-type (WT) and *Trpm1* KO mice (129 Sv/Ev background) were used. For immunohistochemical experiments, 1-mo-old WT, *Trpm1* KO, and *mGluR6* KO mice (129 Sv/Ev background), as well as 1-mo-old WT, *mGluR6* KO, and *Pde6b^{di-2J}/J* (stock #004766; JAX, referred to as *rdl*) mice (C57BL/6J background), were used. Mice of either sex were used. The *Trpm1* KO mouse line, generated by homologous recombination-mediated disruption of the *Trpm1* gene, was provided by Dr. Takahisa Furukawa, Osaka University, Suita, Japan. The *mGluR6* KO mouse line, generated by homologous recombination-mediated disruption of the *mGluR6* gene, was provided by Dr. Shigetada Nakanishi, Kyoto University, Kyoto, Japan. The *rdl* mouse retinas were provided by Dr. Michiko Mandai, Research Center, Kobe City Eye Hospital, Kobe, Japan. Mice were housed in a temperature-controlled room under a 12-h light/12-h dark cycle. Fresh water and diet were always available.

Flat-mount preparation

Mice were dark-adapted overnight prior to electrophysiological experiments. Each mouse was sacrificed by cervical dislocation under a dim red light, and eyes were enucleated. Under a stereomicroscope equipped with an infrared (IR) image converter

(V6833P; Hamamatsu Photonics) and IR illumination (HVL-IRM; Sony), retinas were dissected in a dish filled with Ames' medium (A1372; US Biological or A1420; Sigma-Aldrich) bubbled with 95% O₂/5% CO₂ at room temperature. The retina isolated from the sclera and pigment epithelium was transferred to a recording chamber, and flat-mounted with the ganglion cell layer (GCL) facing upward. The retina was anchored by a platinum horseshoe with fine nylon threads.

Slice preparation

Mice were dark-adapted overnight prior to the procedure. Using an IR image converter and IR illumination, we performed retinal dissection in ice-cold HEPES-buffered solution (130 mM NaCl, 10 mM HEPES, 2.5 mM KCl, 2.5 mM CaCl₂, 1 mM MgCl₂, 28 mM glucose, pH 7.4, with NaOH) continuously bubbled with 100% O₂. Following enucleation, the cornea and lens were carefully removed to create an eyecup. The retina, with the attached retinal pigment epithelium (RPE) and sclera, was cut into quarters and placed RGC side down onto a membrane filter (GSWP04700; Millipore). The RPE and sclera were then gently peeled away from the retina. The retina was subsequently sliced into 200-μm-thick sections using a tissue slicer (EDMS14-234; NARISHIGE). Individual sections were secured in the recording chamber using a platinum horseshoe with fine nylon threads.

Whole-cell recordings

Whole-cell clamp recordings were performed from αRGCs (soma diameter >15 μm) in the flat-mount preparation and from RBCs in the retinal slice preparation. Patch pipettes were filled with either K⁺-based internal solution (125 mM K gluconate, 10 mM KCl, 10 mM HEPES, 10 mM phosphocreatine, 0.5 mM EGTA, 0.05 mM CaCl₂, 2 mM MgCl₂, 5 mM ATP-Na₂, 0.5 mM GTP-Na₃, and 0.2% neurobiotin [NB], pH 7.4, with KOH) for current-clamp recordings in RGCs, or Cs⁺-based internal solution (102 mM CsMeSO₃, 20 mM HEPES, 10 mM phosphocreatine, 5 mM EGTA, 0.5 mM CaCl₂, 2.5 mM MgCl₂, 5 mM ATP-Na₂, 0.5 mM GTP-Na₃, 5 mM QX-314, and 0.2% NB, pH 7.4, with CsOH [E_{Cl} ~ -60 mV]) for voltage-clamp recordings in RGCs. For RBC recordings, only the K⁺-based internal solution was used, in which 50 μM sulforhodamine was included instead of NB.

Recordings were obtained using an EPC 10 amplifier (HEKA; Multi Channel Systems MCS GmbH) controlled by PATCH-MASTER software (version 2.73.5; HEKA). Current and voltage records were sampled at 16 kHz and low-pass-filtered at 2.9 kHz. Patch pipettes were pulled from borosilicate glass capillaries (CNC 1.5; Ken Enterprise, or B150-86-10; Sutter Instrument), using a puller (P97; Sutter Instrument). The resistance of pipettes in Ames' medium was 4–9 MΩ for αRGCs and 9–15 MΩ for RBCs. A correction was made for liquid junction potential (~10 mV). The retina was continuously superfused with Ames' medium bubbled with 95% O₂/5% CO₂ at the rate of 2.5 ml/min at 32°C.

Light stimulation

In recordings from flat-mount preparation, a light stimulus was projected from a DLP projector (L51W, refresh rate 60 Hz, 1,280 × 1,024 pixels; NEC), in which the projection lens was replaced

with an achromatic lens ($f = 120$ mm). The image was focused onto the photoreceptor layer through an objective lens ($4\times$ Plan Achromat; Nikon), after removing the condenser lens of an upright microscope (Axio Examiner D1; Zeiss). The retina was stimulated with a white spot (diameter: $300\ \mu\text{m}$) for 2 s ($0.26\ \text{cd}/\text{m}^2$) on a dark background ($0.0012\ \text{cd}/\text{m}^2$) every 10 s. Luminance was measured by a luminance meter (CS-150; KONICA MINOLTA).

In recordings from slice preparation, retinal images were observed using the upright microscope with IR differential interference contrast (DIC) optics.

Cell identification

Following recordings, retinas were fixed in 4% paraformaldehyde in 0.1 M phosphate buffer for 1 h at room temperature. They were then rinsed several times in phosphate-buffered saline (PBS) and incubated overnight at 4°C in a blocking solution (4% normal donkey serum, 0.5% Triton X-100, and 0.1% sodium azide in PBS). Retinas were subsequently incubated with primary antibodies in the blocking solution for 7 days at 4°C . After washing with PBS, retinas were incubated with secondary antibodies for 2 days at 4°C . After washing with PBS, retinas were mounted onto microscope slides. Primary antibodies were goat anti-choline acetyltransferase (ChAT, 1:100, AB144P; Sigma-Aldrich) and mouse anti-SMI-32 (1:1,000, 801701; BioLegend). Secondary antibodies were streptavidin-Alexa 488 (1:500, S32354; Invitrogen), donkey anti-goat Alexa 568 (1:500, A-11057; Invitrogen), and donkey anti-mouse Alexa 647 (1:500, A-31571; Invitrogen).

Z-stack images ($1,024 \times 1,024$ pixels, $0.3\ \mu\text{m}/\text{slice}$) were acquired by a confocal microscope (LSM900; Zeiss) equipped with $40\times$ objective lens (Plan-APOCHROMAT $40\times/0.95$ CORR M27; Zeiss). Images were analyzed using ImageJ (version 1.53t; National Institutes of Health) and custom codes written in Python. Among recorded RGCs, SMI-32-positive cells with a large soma size ($>15\ \mu\text{m}$) were identified as α RGCs (Krieger et al., 2017). These α RGCs were further subclassified into OFF or ON types based on their dendritic stratification relative to ChAT bands in the IPL.

The cell intracellularly filled with sulforhodamine was identified as RBCs based on the soma location within the inner nuclear layer (INL) and on the position and morphology of axon terminals in the IPL.

Pharmacology

Pharmacological agents dissolved in Ames' medium were bath-applied: DNQX ($100\ \mu\text{M}$; Sigma-Aldrich) for blocking AMPA/KA glutamate receptors; D-AP5 ($50\ \mu\text{M}$; Tocris Bio-Techne) for blocking NMDA glutamate receptors; MFA ($100\ \mu\text{M}$; Sigma-Aldrich) for blocking gap junctions; strychnine ($10\ \mu\text{M}$; Sigma-Aldrich) for blocking glycine receptors.

Data analysis

All data analyses were performed using Python. The power spectral density (PSD) was calculated from the autocorrelogram of spike events recorded during a 145-s membrane potential trace under the current-clamp mode. For the PSD and the autocorrelogram, 0.5-Hz bin width and 1-ms bin width were used,

respectively. Oscillation frequency was defined as the frequency corresponding to the peak power between 1.5 and 30 Hz in the PSD. The cross-correlogram (CCR) was calculated based on the spike timing between a pair of RGCs. The time lag was converted to phase by referencing the fundamental frequency of oscillations in each RGC pair.

The amplitude of spontaneous synaptic currents under the voltage-clamp mode was analyzed as follows. The current trace was band-pass-filtered (Bessel filter; 1–100 Hz), and the trace during the last 2.5 s of a 3-s voltage step was used to generate a current histogram with 5-pA bin width. A cumulative distribution function (CDF) was then calculated from the histogram. The current amplitude was defined as the distance between 0.05 and 0.95 in the CDF. The polarity of synaptic current was determined by the value of skewness of the current histogram (i.e., the inward and outward currents were less than -0.15 and >0.15 , respectively, whereas the values in between were not used for analysis). The reversal potential of the synaptic current was estimated from the current amplitude–voltage relationship. The PSD of spontaneous synaptic current was calculated using a bin width of 0.5 Hz from the band-pass-filtered trace.

The membrane potential of RBCs was recorded for 40 s under the current-clamp mode, and the voltage histogram was constructed using a bin width of 1 mV. The resting membrane potential was defined as the membrane potential corresponding to the peak value of the histogram. For voltage-clamp recordings, cells were held at $-60\ \text{mV}$ and stepped from -80 to $0\ \text{mV}$ in $+10\ \text{mV}$ increments to construct current–voltage (I–V) curves. The slope conductance was subsequently calculated from the linear portion of the I–V curve, specifically near the resting membrane potential.

Immunohistochemistry

Mice were euthanized by cervical dislocation, and the eyes were enucleated. In a dish filled with PBS, the cornea and lens were removed, and the retinas were isolated from the eyecups. Retinas were fixed in 4% paraformaldehyde in 0.1 M phosphate buffer for 20 min at room temperature. After washing with PBS, the retinas were embedded in 4% low-melting agarose (NIPPON GENE) in PBS. Retinas were sectioned at $50\text{-}\mu\text{m}$ thickness using a vibratome (PRO7; Dosaka EM) and incubated in PBS containing either 5% normal goat serum or 5% normal donkey serum, both with 0.1% Triton X-100, for 1 h at room temperature. After blocking, sections were incubated with primary antibodies overnight at 4°C . After washing with PBS, the sections were then incubated with secondary antibodies. Sections were rinsed several times with PBS and mounted on microscope slides. The primary and secondary antibodies used are listed in Table 1.

Z-stack images ($1,024 \times 1,024$ pixels, $0.2\ \mu\text{m}/\text{slice}$) were acquired by the confocal microscope equipped with a $63\times$ oil immersion lens (Plan-APOCHROMAT $63\times/1.4$ Oil DIC M27, Zeiss). Voxel size was $0.1 \times 0.1 \times 0.2\ \mu\text{m}$ per pixel. Image analyses were performed using ImageJ, Imaris (ver. 9.9.1; Oxford Instruments), and Python. The volume of RBC axon terminals was measured from the merged volume of PKC α and VGLUT1 signals. The distributions of RBC axon terminals and type 6 BC axon terminals in the IPL were defined as the starting point (INL side) and

Table 1. Antibodies

Antibodies	Source	Cat	Dilution
Guinea pig anti-mGluR6	Lab-made (Ueno et al., 2025, Preprint)	N/A	1:5,000
Mouse anti-CtBP2	BD Biosciences	612044	1:1,000
Mouse anti-PKCa	Sigma-Aldrich	P5704	1:3,000
Mouse anti-Syt2	Developmental Studies Hybridoma Bank	Znp-1	1:1,000
Sheep anti-TRPM1	Courtesy of Dr. Kirill Martemyanov	N/A	1:500
Rabbit anti-cone arrestin	Sigma-Aldrich	AB15282	1:1,000
Goat anti-GluK1	Courtesy of Dr. Steven H. DeVries, Northwestern University, Evanston, IL, USA	N/A	1:1,000
Goat anti-ChAT	Sigma-Aldrich	AB144P	1:50
Guinea pig anti-VGluT1	Sigma-Aldrich	AB5905	1:6,000
Goat anti-guinea pig IgG-Alexa 488	Invitrogen	A-11073	1:500
Goat anti-mouse IgG-Alexa 555	Invitrogen	A-21425	1:500
Donkey anti-mouse IgG-Alexa 488	Jackson ImmunoResearch	715-545-151	1:500
Donkey anti-sheep IgG-Alexa 555	Invitrogen	A-21436	1:250
Donkey anti-rabbit IgG-Alexa 488	Jackson ImmunoResearch	711-545-152	1:500
Donkey anti-guinea pig IgG-Alexa Cy3	Jackson ImmunoResearch	706-165-148	1:500
Donkey anti-goat IgG-Alexa 647	Abcam	ab150139	1:500
Donkey anti-mouse IgG-Alexa 488	Abcam	ab181289	1:500
Donkey anti-mouse IgG-Alexa 647	Molecular Probes	A31571	1:500
Donkey anti-goat IgG-Alexa 568	Invitrogen	A-11057	1:500
DAPI	Sigma-Aldrich	D8417	1:10,000

ending point (GCL side) of PKCa signal distribution and Syt2 signal distribution by eye, and it was evaluated relative to the ChAT bands (OFF band: 0%; ON band: 100%).

Computer simulations

Retinal neural circuit models were constructed to reproduce not only the normal firing of RGCs in WT retinas but also the spontaneous oscillatory firing of RGCs observed in pathological retinas. The following three steps were involved in the simulation. (1) Construction of a normal retinal neural circuit model

(the WT circuit model): based on the experimental data obtained from WT retinas, we constructed a model that responded to both the offset and onset of light stimuli (Dunn et al., 2006; Margolis and Detwiler, 2007; Arman and Sampath, 2012). (2) Application of known pathological conditions: pathological conditions identified in previous studies (Chua et al., 2009; Koike et al., 2009; Križaj et al., 2010; Takeuchi et al., 2018) were applied to the WT mouse model constructed in step 1). Additionally, certain pathological conditions observed in the present study were also incorporated. (3) Exploration of conditions leading to RGC oscillations: based on the pathological model constructed in step 2, we explored the conditions under which RGCs exhibited pathological spontaneous oscillatory firing.

The retinal neural circuit model was implemented using the following neuron and synapse models. *Neuron models*: BCs (RBC, OFF CBC, and ON CBC) (Usui et al., 1996), AII AC (Choi et al., 2014), and RGCs (OFF and ON RGCs) (Fohlmeister et al., 2010). The BC model was simplified from a multicompartment model to a single-compartment model, whereas the other neuron models were used as originally described. *Synapse models*: electrical synapses, conventional synapses, and ribbon synapses. In the ribbon synapse model, synaptic vesicles belonged to one of four states (Fig. S1) and underwent state transitions according to Eqs. 1, 2, 3, 4, and 5.

$$\frac{dP_3}{dt} = \frac{A}{\tau_{A3}} - \frac{P_3(P_{2,max} - P_2)}{\tau_{32}} \quad (1)$$

$$\frac{dP_2}{dt} = \frac{P_3(P_{2,max} - P_2)}{\tau_{32}} - \frac{P_2(P_{1,max} - P_1)}{\tau_{21}} \quad (2)$$

$$\frac{dP_1}{dt} = \frac{P_2(P_{1,max} - P_1)}{\tau_{21}} - \frac{uP_1}{\tau_{1A}} \quad (3)$$

$$\frac{dA}{dt} = \frac{uP_1}{\tau_{1A}} - \frac{A}{\tau_{A3}} \quad (4)$$

$$u = \frac{1}{2} \left[1 + \tanh \left(\frac{V_{pre} - V_{th}}{V_{slp}} \right) \right] \quad (5)$$

Here, τ_{1A} , τ_{A3} , τ_{32} , τ_{21} , $P_{1,max}$, $P_{2,max}$ are kinetic parameters (Table S1), and u represents the release probability of presynaptic neurotransmitter, which is determined by the activation function of the presynaptic membrane potential: V_{pre} , V_{th} and V_{slp} are the presynaptic membrane potential, the half voltage for activation of Ca^{2+} channels, and the slope of activation function of Ca^{2+} channels, respectively. This presynaptic action is similar to the previous model (Schröder et al., 2021). In addition to the presynaptic action, our model incorporated the postsynaptic action (Eq. S5 in the supplemental text at the end of the PDF). We confirmed that this synapse model could reproduce the kinetics of ribbon synapses (Fig. S2) (Grabner et al., 2016). The connection patterns and number of connections for each cell were determined based on the findings of previous studies (Jeon et al., 1998; Tsukamoto et al., 2001; Veruki and Hartveit, 2002; Margolis and Detwiler, 2007; Völgyi et al., 2009; Arai et al., 2010; Arman and Sampath, 2012; Tsukamoto and Omi, 2013, 2017; Baden et al., 2016) as summarized in Table S2. In this model, photoreceptor cells were not included, but light stimulation was incorporated as input currents to the BC model that mimicked the synaptic currents evoked by photoreceptors, i.e., a hyperpolarizing current to OFF CBCs and a depolarizing

current to RBCs and ON CBCs. The source codes of the proposed models are registered to ModelDB (<https://modeldb.science/2019896>) and GitHub (<https://github.com/ktnrkt/InnerRetina/tree/master>).

For comparison with experimental results, the retinal neural circuit models were modified by setting the input currents to BCs:

- The WT circuit model: the input currents representing photoreceptor signals were applied to all BC types.
- The *Trpm1* KO circuit model: TRPM1 channels are expressed only on the dendrites of ON BCs (RBCs and ON CBCs). We hypothesized that light signals are not transmitted to downstream cells in the ON pathway due to the absence of TRPM1 function. Consistent with this hypothesis, we found that the membrane potential of RBCs is hyperpolarized in these mice (Fig. 4, A and B). Therefore, sustained hyperpolarizing currents were applied to RBCs to induce hyperpolarization, whereas no input currents were applied to ON CBCs. Input currents representing photoreceptor signals comparable to those in the WT circuit model were applied to OFF CBCs.
- The *mGluR6* KO circuit model: mGluR6 is also expressed only on the dendrites of ON BCs. Loss of mGluR6 leads to hyperpolarization of RBCs (Xu et al., 2012). Therefore, we assume that BCs in the *mGluR6* KO model behave similar to those in the *Trpm1* KO circuit model. As in the *Trpm1* KO circuit model, sustained hyperpolarizing currents were applied to RBCs to induce hyperpolarization, whereas no input currents were applied to ON CBCs. Input currents representing photoreceptor signals comparable to those in the WT circuit model were applied to OFF CBCs.
- The *rdl* circuit model: in the *rdl* mouse retina, photoreceptor degeneration leads to the loss of glutamate release from photoreceptors and the loss of TRPM1 channels in ON BC dendrites (Fig. 3 N) (Križaj et al., 2010). Based on these alterations, the hyperpolarization observed in RBCs in the *Trpm1* KO mouse retina (Fig. 4), and a previous report showing a similar state in the *rdl* mouse retina (Borowska et al., 2011), we hypothesized that RBCs are also hyperpolarized in the *rdl* mouse retina. As in the *Trpm1* KO and *mGluR6* KO circuit models, sustained hyperpolarizing currents were applied to RBCs to induce hyperpolarization. No input currents were applied to OFF and ON CBCs.

In addition, we imposed the conditions based on the experimental evidence (2) and explored the conditions where oscillatory firing was evoked in appropriate RGCs (3).

A detailed description of the computational simulation is provided in the supplemental text at the end of the PDF.

Statistical analysis

Data were presented as the mean \pm SEM, except for immunohistochemical data, which were presented as the mean \pm SD. Error bars indicate SEM unless otherwise noted. For pharmacological data, statistical significance was evaluated using a two-sided paired *t* test. For immunohistochemical data, multiple comparisons were performed using one-way ANOVA with post hoc Tukey's test. Other comparisons were made using two-sided unpaired Student's *t* test. A *P* value <0.05 was considered

statistically significant (n.s., not significant; $^*P < 0.05$; $^{**}P < 0.01$; $^{***}P < 0.001$).

Online supplemental material

Fig. S1 illustrates the states of neurotransmitters of a ribbon synapse and the transition between them. Fig. S2 displays time courses of response recovery of the ribbon synapse model. Table S1 summarizes parameters values of the ribbon synapse model. Table S2 summarizes parameters of synaptic connectivity between cells and synaptic conductance, and the values of the synaptic conductance (the upper row in each cell) and the connectivity ratio (pre:post; the bottom row in each cell). Supplemental text at the end of the PDF contains a detailed description of the computational simulation used in this paper.

Results

Identification of aRGC subtypes in the *Trpm1* KO mouse

Previous MEA recordings demonstrated that RGCs of the *Trpm1* KO mouse retina generate spontaneous oscillatory firing (Takeuchi et al., 2018). To elucidate the mechanism underlying these oscillations, we performed whole-cell recordings from aRGCs (soma size >15 μ m) in flat-mount retinas of *Trpm1* KO mice. It should be noted that ON BCs do not respond to light illumination due to the deletion of TRPM1 channels. Whole-cell current-clamp recordings revealed that spot illumination elicited OFF responses in some aRGCs (Fig. 1 A, left), while others showed no light responses (Fig. 1 B, left). To confirm that the light-responsive and nonresponsive cells corresponded to OFF and ON aRGCs, respectively, we examined the morphology of RGCs filled with NB through a recording pipette. RGC subtypes were determined by their dendritic stratification relative to the ChAT bands (dendritic stratification of OFF and ON starburst ACs) in the IPL. The OFF- and ON-ChAT bands in the IPL were defined as 0% and 100%, respectively. Consistent with their light responses, RGCs with light-Off responses had dendrites that stratified in the OFF sublamina (Fig. 1 A, center), whereas those without responses stratified their dendrites in the ON sublamina (Fig. 1 B, center). Furthermore, immunohistochemical staining for SMI-32, an aRGC marker, confirmed that the recorded RGCs were indeed aRGCs (Fig. 1, A and B, right, arrowheads). Therefore, in the following experiments, the subtype of recorded RGCs was determined based on this postrecording morphological analysis.

Fundamental frequency of oscillations in OFF aRGCs was similar to that in ON aRGCs

To examine the properties of spontaneous oscillatory discharges in aRGCs, cells were whole-cell current-clamped using a patch pipette filled with K⁺-based solution. Spike discharges were evoked when the membrane potential fluctuations reached a threshold (Fig. 1 C, left). An autocorrelogram was calculated from the timing of these spike discharges (Fig. 1 C, center). The PSD derived from the autocorrelogram revealed that the fundamental frequency of oscillations was \sim 8–9 Hz (Fig. 1 C, right) in both OFF and ON aRGCs (Fig. 1 D). These results may be explained either by common inputs from a presynaptic oscillator or by their own similar intrinsic oscillators.

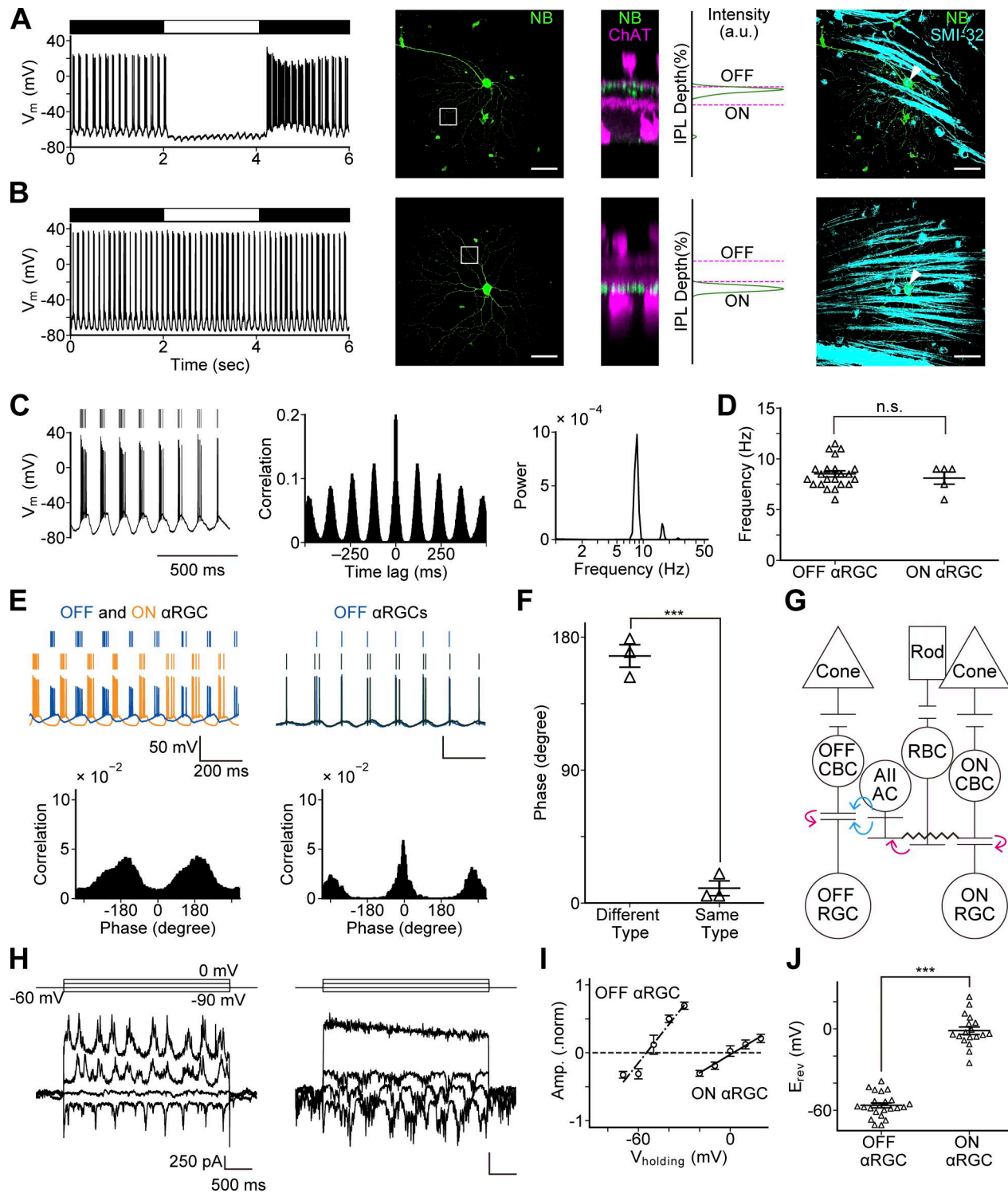


Figure 1. Identification of aRGC subtypes and characterization of their oscillatory properties. **(A)** Light-evoked response and morphology of an OFF aRGC. Membrane potential change to light stimulation in an OFF aRGC (left). Whole-mount view of an OFF aRGC (center). The white rectangle indicates an ROI. Side view of the stacked NB and ChAT images in the ROI. A plot of labeling intensity versus IPL depth indicates that dendritic arborization of the OFF aRGC (NB: green) is relative to the position of ChAT bands (magenta) in the ROI. The OFF aRGC dendrites stratify in the OFF sublamina. Whole-mount view of the stacked NB-stained OFF aRGC image (green) and SMI-32 images (cyan) (right). The white arrowhead indicates colocalization of the OFF aRGC soma with the SMI-32 signal. **(B)** Light response and morphology of an ON aRGC. No obvious light-evoked response was observed in an ON aRGC (left). Morphological analysis in an ON aRGC (center). The ON aRGC dendrites stratify in the ON sublamina. Whole-mount view of the stacked ON aRGC image (green) and SMI-32 images (cyan) (right). Scale bar: 50 μ m. **(C)** RGC oscillations in the *Trpm1* KO mouse retina. Membrane potential trace from an OFF aRGC under the current-clamp condition (left). Spike events (top) and voltage trace (bottom). Autocorrelogram (center) is calculated from the spike events (left). The PSD (right) is derived from the autocorrelogram (center). A clear peak was detected at 8.5 Hz. **(D)** The frequency of oscillations in OFF and ON aRGCs (OFF aRGCs: 8.5 \pm 0.3 Hz, n = 22 cells; ON aRGCs: 7.5 \pm 0.3 Hz, n = 15 cells). **(E)** Autocorrelogram for OFF and ON aRGCs. **(F)** Phase plot showing phase difference between different and same types of aRGCs. *** indicates significant difference. **(G)** Schematic of the retinal circuit showing the connection between Cone, Rod, OFF CBC, AII AC, RBC, ON CBC, OFF RGC, and ON RGC. **(H)** Current-clamp recordings showing membrane potential change. **(I)** Scatter plot of Amp. (norm) vs $V_{holding}$ (mV) for OFF and ON aRGCs. **(J)** Scatter plot of E_{rev} (mV) for OFF and ON aRGCs. *** indicates significant difference.

from nine mice; ON α RGCs: 8.1 ± 0.6 Hz, $n = 5$ cells from five mice; $P = 0.55$). (E) Phase relationship of oscillatory firing between α RGC pairs. Top: Membrane potential changes (bottom) and spike events (top) obtained from a pair of OFF (blue) and ON (orange) α RGCs (left), and from a pair of OFF (blue) and OFF (black) α RGCs (right). Bottom: CCRs calculated from the spike events. (F) Phase difference of α RGC oscillations: different-type: $167.3 \pm 7.6^\circ$, $n = 3$ cell pairs from three mice; same-type: $10.0 \pm 5.0^\circ$, $n = 3$ cell pairs from two mice; $P = 1.89 \times 10^{-5}$. (G) Schematic diagram of the rod pathway including an AII AC. Excitatory (magenta) and inhibitory (cyan) synapses, as well as gap junction (—), are illustrated. (H) Synaptic currents (bottom) measured at different holding potentials (top) from an OFF α RGC (left) and an ON α RGC (right) under the whole-cell voltage-clamp condition. (I) Amplitude of synaptic currents at different holding potentials (OFF α RGCs: $n = 23$ cells from 19 mice; ON α RGCs: $n = 18$ cells from 16 mice). (J) Reversal potentials of oscillatory synaptic currents in OFF and ON α RGCs (OFF α RGCs: -56.4 ± 1.8 mV, $n = 23$ cells from 19 mice; ON α RGCs: -1.3 ± 2.8 mV, $n = 18$ cells from 16 mice; $P = 8.03 \times 10^{-20}$). Data are presented as the mean \pm SEM. An unpaired *t* test was used for statistical analysis. n.s., not significant; *** $P < 0.001$. ROI, region of interest.

Phase of oscillations was anti-phase in a pair of different α RGC types

To examine the phase relationship of oscillations, we performed simultaneous whole-cell current-clamp recordings from pairs of α RGCs. CCRs were calculated from their spike discharges, and the time lag was converted to phase using the fundamental frequency of oscillations in each RGC pair (Fig. 1 E). The phase of oscillations was anti-phase between a pair of OFF and ON α RGCs, whereas it was in-phase between a pair of the same α RGC type. This difference in phase relationship was statistically significant (Fig. 1 F). These findings are consistent with those previously reported in *rdl* and *Nyx^{nob}* mouse retinas (Margolis et al., 2014; Winkelman et al., 2019), and suggest the idea that oscillations in OFF and ON α RGCs are driven by synaptic inputs from common presynaptic oscillators.

OFF and ON α RGC oscillations were generated by different synaptic inputs

To determine whether α RGC oscillations were driven by synaptic inputs rather than intrinsic voltage-dependent membrane properties, α RGCs were whole-cell voltage-clamped using a patch pipette filled with Cs⁺-based solution to suppress K⁺ channels. Under these conditions, oscillatory membrane currents were evident, indicating that the oscillations were indeed driven by synaptic inputs rather than intrinsic properties of α RGCs. The mean frequency of these synaptic current oscillations was 3.1 ± 0.2 Hz ($n = 41$ cells from 28 mice), which was significantly lower than that observed during current-clamp recordings with K⁺-based pipette solution (8.5 ± 0.3 Hz, $n = 27$ cells from 9 mice) ($P = 4.64 \times 10^{-26}$, unpaired Student's *t* test). This frequency difference might be attributable to the blockade of I_h channels (Kaneko and Tachibana, 1985; Müller et al., 2003; Trenholm et al., 2012) and/or M-type K⁺ channels (Cembrowski et al., 2012; Choi et al., 2014) by Cs⁺ extruded from a patch pipette before establishing the cell-attached configuration.

To further characterize the oscillatory synaptic inputs, synaptic currents were recorded at various holding potentials in both OFF and ON α RGCs (Fig. 1 H). The amplitudes of these synaptic currents (see Materials and methods) were plotted against their corresponding holding potentials (Fig. 1 I). The reversal potential of the synaptic currents differed significantly between OFF and ON α RGCs (Fig. 1 J). These results suggest that oscillations in OFF α RGCs are driven by inhibitory (glycinergic and/or GABAergic) synaptic inputs, while those in ON α RGCs are driven by excitatory (glutamatergic) synaptic inputs. The observed differences in synaptic inputs are consistent with the known retinal circuitry involving AII ACs. AII ACs form gap

junctions with both ON CBCs and other AII ACs and make glycinergic synapses onto OFF CBCs and some OFF RGCs (Fig. 1 G) (Feigenspan et al., 2001; Murphy and Rieke, 2006; Murohy and Rieke, 2008; Münch et al., 2009; Tsukamoto and Omi, 2017). Therefore, it is likely that OFF α RGCs receive direct glycinergic inputs from AII ACs, whereas ON α RGCs may receive glutamatergic inputs from ON CBCs, which are connected to AII ACs through gap junctions (Fig. 1 G).

Blockade of AII AC pathways eliminates oscillatory synaptic currents in α RGCs

We conducted pharmacological experiments to investigate the synaptic pathways responsible for transmitting oscillatory signals to α RGCs. OFF α RGCs were voltage-clamped at 0 mV to isolate oscillatory postsynaptic currents (IPSCs). Bath application of strychnine (10 μ M), a glycine receptor antagonist, significantly reduced both the amplitude of IPSCs and the peak power in the PSD (Fig. 2, A and D). In contrast, application of iGluR antagonists (a mixture of 100 μ M DNQX and 50 μ M D-AP5) affected neither the amplitude of IPSCs nor the peak power in the PSD (Fig. 2, B and D). This result suggests that oscillatory IPSCs in OFF α RGCs may be driven directly by AII ACs rather than via other ACs through iGluR-mediated synapses. Application of MFA (100 μ M), a nonspecific gap junction blocker, also significantly reduced both the amplitude of IPSCs and the peak power in the PSD (Fig. 2, C and D). Based on the circuit diagram shown in Fig. 1 G, the effects of glycine receptor and iGluR antagonists were consistent with expectations. However, the effect of the gap junction blocker was unexpected. It is possible that gap junction blockade hyperpolarizes AII ACs and abolished oscillatory activity in AII ACs themselves (see Fig. 7 C) (Trenholm et al., 2012; Choi et al., 2014).

ON α RGCs were voltage-clamped at -60 mV to record oscillatory excitatory postsynaptic currents (EPSCs). Application of strychnine (10 μ M) affected neither the amplitude of EPSCs nor the peak power in the PSD (Fig. 2, E and H). In contrast, application of iGluR antagonists (a mixture of 100 μ M DNQX and 50 μ M D-AP5) abolished both the oscillatory EPSCs and the peak power in the PSD (Fig. 2, F and H). MFA (100 μ M) also significantly reduced the amplitude of EPSCs and the peak power in the PSD (Fig. 2, G and H). These findings are consistent with the synaptic connections outlined in Fig. 1 G.

Position and size of RBC axon terminals

Previous studies have shown that both *Trpm1* KO and *rdl* mouse retinas exhibit prominent spontaneous oscillations in RGCs, whereas the *mGluR6* KO mouse retina shows infrequent or

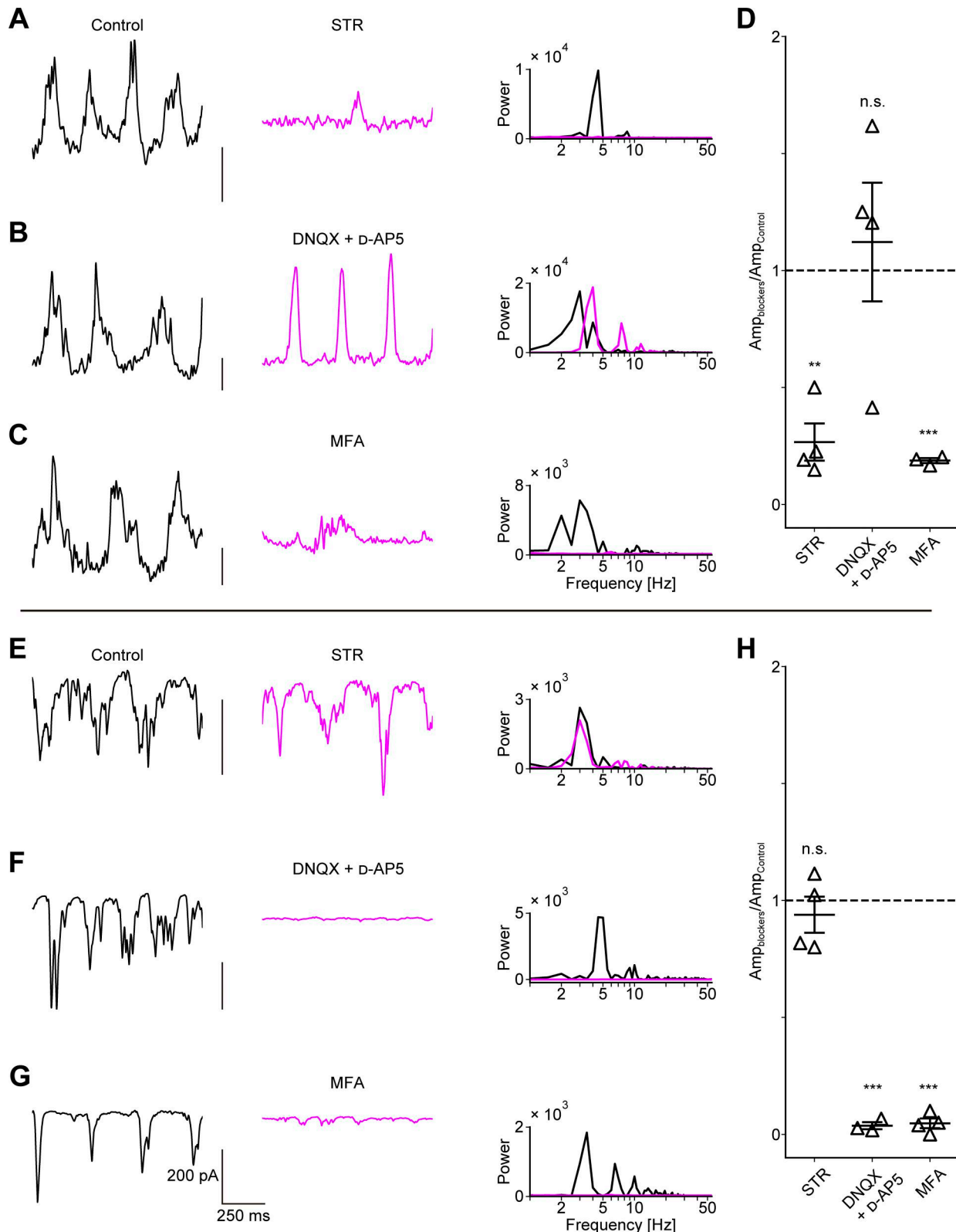


Figure 2. Oscillatory synaptic currents are eliminated by blockers, which affect the pathways involving All AC. (A–C) Effects of synaptic blockers on IPSCs in OFF aRGCs. IPSCs recorded from OFF aRGCs in the control condition (left). Effects of blockers on IPSCs in the presence of blockers (center). PSDs in the control condition (black) and blocker conditions (magenta) (right). **(D)** Ratios of IPSC amplitudes in the presence of blockers to those under control conditions in OFF aRGCs (STR: 0.27 \pm 0.08, n = 4 cells from three mice; P = 2.69 \times 10⁻³, DNX + D-AP5: 1.12 \pm 0.25, n = 4 cells from four mice; P = 0.66, MFA: 0.19 \pm 0.01, n = 3 cells from three mice; P = 1.71 \times 10⁻⁴). **(E–G)** Effects of synaptic blockers on EPSCs in ON aRGCs. Layouts and analyses are the same as in A–C. **(H)** Ratios of EPSC amplitudes in the presence of blockers to those under control conditions in ON aRGCs (STR: 0.94 \pm 0.08, n = 4 cells from three mice; P = 0.49, DNX + D-AP5: 0.04 \pm 0.01, n = 3 cells from three mice; P = 2.42 \times 10⁻⁴, MFA: 0.05 \pm 0.02, n = 4 cells from four mice; P = 2.22 \times 10⁻⁵). Data are presented as the mean \pm SEM. A paired t test was used for statistical analysis. n.s., not significant; **P < 0.01; ***P < 0.001. STR: strychnine.

absent spontaneous oscillations (Margolis et al., 2008; Margolis et al., 2014; Stasheff, 2008; Borowska et al., 2011; Menzler and Zeck, 2011; Yee et al., 2012; Choi et al., 2014; Poria and Dhingra, 2015; Takeuchi et al., 2018; Hasan et al., 2020). In the WT mouse retinas, RBCs, which express both TRPM1 and mGluR6 on their dendritic membranes, provide glutamatergic output to AII ACs. Thus, it is interesting to examine whether the morphological features of RBC differ among these mouse retinas. Firstly, we focused on the position and size of RBC axon terminals. We examined the distribution of RBC terminals relative to ChAT bands in the IPL in each mouse retina. The starting point of terminal distribution in the distal IPL did not significantly differ among WT, *Trpm1* KO, and *mGluR6* KO mouse retinas (Fig. 3, A–C). However, the ending point of terminal distribution in the proximal IPL was significantly closer to the ON-ChAT band (100%) in the *Trpm1* KO mouse retinas compared with both WT and *mGluR6* KO mouse retinas (Fig. 3, A–C).

To determine whether this change in terminal distribution is specific to RBCs or common among ON BCs, we compared the distribution of type 6 BC terminals between WT and *Trpm1* KO mouse retinas. No significant difference was found in the terminal distribution of type 6 BCs between the two genotypes. In contrast, RBC terminals in the *Trpm1* KO mouse retinas showed a significantly shorter span, with their ending point located closer to the ON-ChAT band than in the WT mouse retinas (Fig. 3, D–F). These results suggest that the altered distribution of RBC terminals in the *Trpm1* KO mouse retinas is cell type-specific and not simply due to a general change in the thickness of the ON sublamina. In the *rdl* mouse retinas, the RBC terminal distribution was shifted toward the INL side (Fig. 3, G–I).

We previously reported that the volume of individual RBC axon terminals is reduced in the *Trpm1* KO mouse retinas relative to the *mGluR6* KO and WT mouse retinas, which are indistinguishable (Takeuchi et al., 2018). In the *rdl* mouse retina, a similar reduction in RBC axon terminal volume was observed (Fig. 3, J and K) (see also Strettoi et al., 2002, 2003; Chua et al., 2009). Together, these results demonstrate that prominent alterations in RBC axon terminals are present in both *Trpm1* KO and *rdl* mouse retinas, but not in the *mGluR6* KO mouse retinas. It is tempting to speculate that these morphological alterations are associated with a reduction in signaling from RBCs to AII ACs in both *Trpm1* KO and *rdl* mouse retinas.

Marker expression in the outer plexiform layer

In the outer plexiform layer (OPL), knocking out *Trpm1* affected neither the intensity of mGluR6 puncta nor their apposition to the presynaptic rod ribbon marker rib eye (CtBP2) (Fig. 3 L), consistent with previous reports (Koike et al., 2009; Morgans et al., 2009). Similarly, knocking out *Trpm1* did not alter the colocalization of mGluR6 with GluK1 (a kainate receptor subunit: OFF CBC marker) and arrestin at cone terminals (Fig. 3 M). In contrast, the localization of TRPM1 in the OPL differed among WT and three models (*Trpm1* KO, *mGluR6* KO, and *rdl*) (Fig. 3 N). In the *mGluR6* KO mouse retinas, TRPM1 puncta were present but displayed slightly reduced intensity compared with the WT mouse retinas. In the *rdl* mouse retinas, TRPM1 puncta on RBC dendrites were markedly reduced (Fig. 3 N). This finding was

consistent with the loss of rod spherules, although some cone pedicles were preserved (Fig. 3 O). The *Trpm1* KO mouse retina lacks puncta by definition (Koike et al., 2009; Morgans et al., 2009). These results suggest a three-way association with RGC oscillations: the extent of TRPM1 loss at dendrites, the altered distribution of RBC terminals, and the shrinkage of RBC axon terminals.

RBC membrane potential was hyperpolarized in the *Trpm1* KO mouse retina

Our immunohistochemical analyses revealed morphological alterations of RBCs in mouse retinas that exhibit RGC oscillations. Based on these findings, we next investigated potential functional changes, specifically focusing on the synaptic input from RBCs to AII ACs. It seems likely that the neurotransmitter release from neurons, including RBCs, depends on their membrane potential (Snellman et al., 2009; Graydon et al., 2018). Thus, using retinal slice preparation, we measured the resting membrane potential of RBCs. The resting membrane potential of RBCs in the *Trpm1* KO mouse retinas was significantly hyperpolarized compared with those in the WT mouse retinas (Fig. 4, A and B). This may result from the loss of the TRPM1 channels. To test this possibility, we analyzed the I–V relationship of RBCs. We found that the slope conductance, calculated from the linear range of the I–V curve (Fig. 4 C) near the resting membrane potential, was significantly lower in the *Trpm1* KO mouse retinas than in the WT mouse retinas (Fig. 4 D). Therefore, the hyperpolarization of RBCs in the *Trpm1* KO mouse retinas may cause reduced glutamate release from RBCs to AII ACs.

Reproduction of oscillations based on common morphological alterations in the *Trpm1* KO and *rdl* mouse retinas

We constructed retinal circuit models to examine whether reduced synaptic input from RBCs to AII ACs can generate oscillatory firing in RGCs. First, we developed a normal retinal circuit model (the WT circuit model) as described in Materials and methods (see also supplemental text at the end of the PDF). Second, we modified the input currents to BCs in each mouse circuit model to reproduce the light-evoked responses, as detailed in Materials and methods (see also supplemental text at the end of the PDF). Third, to reflect the shrinkage of RBC axon terminals observed in the *Trpm1* KO and *rdl* mouse retinas (Fig. 3) (Takeuchi et al., 2018), we reduced the synaptic conductance from RBCs to AII ACs in those circuit models.

In the mammalian retina, RBCs provide excitatory drive to AII ACs, which in turn are electrically coupled to ON CBCs via gap junctions (Fig. 1 G). In the *Trpm1* KO and *rdl* mouse retinas, the loss of TRPM1 channels induces severe defects in RBCs, including its absence or a marked reduction of the channel at their dendritic tips (Koike et al., 2009) (Fig. 3 N), altered axon terminal morphology (Takeuchi et al., 2018) (Fig. 3), and a hyperpolarized resting membrane potential (Fig. 4) (Borowska et al., 2011). Collectively, these deficits are expected to reduce the excitatory drive to AII ACs, consequently leading to a hyperpolarizing shift in the resting membrane potential of the coupled ON CBCs. Furthermore, the loss of the light-evoked responses in ON CBCs in these mouse retinas may also contribute to their

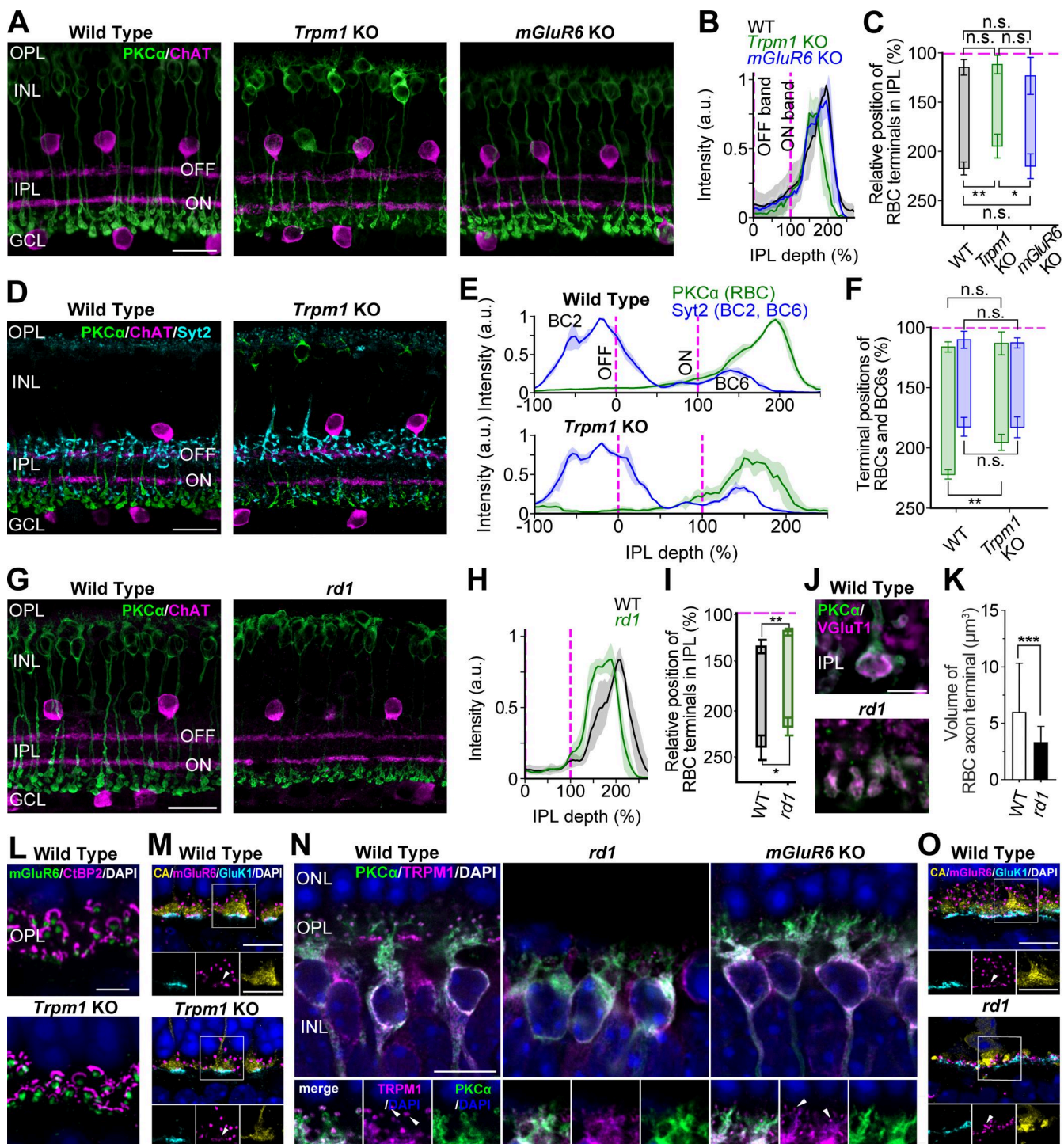


Figure 3. Common morphological features and marker expression in the *Trpm1* KO and *rd1* mouse retinas. (A–C) Distribution of RBC terminals in the WT, *Trpm1* KO, and *mGluR6* KO mouse retinas. (A) RBCs and SACs were immunolabeled with PKCa (green) and ChAT (magenta; IPL sublaminar marker), respectively. Scale bar: 20 μm . (B) Intensity profiles of RBC labeling from A relative to the location of the ChAT bands (magenta dotted lines). Solid lines and shaded areas represent the mean \pm SD, respectively. (C) Ending point of RBC terminal distribution in the IPL was significantly shifted toward the ON-ChAT band (magenta dotted lines) in the *Trpm1* KO mouse retinas compared with the WT and *mGluR6* KO mouse retinas (starting point: WT: 114.6 \pm 7.9%, n = 6 sections from six mice; *Trpm1* KO: 111.8 \pm 9.3%, n = 5 sections from five mice; *mGluR6* KO: 123.3 \pm 18.8%, n = 3 sections from three mice; P = 0.24, ending point: WT: 217.3 \pm 6.6%, n = 6 sections from six mice; *Trpm1* KO: 194.6 \pm 12.1%, n = 6 sections from six mice; *mGluR6* KO: 215.1 \pm 12.5%, n = 3 sections from three mice; P = 0.004). (D–F) Distribution of RBC and type 6 BC terminals in the WT and *Trpm1* KO mouse retinas. (D) RBCs, type 2 and 6 BCs, and SACs were immunolabeled with PKCa (green), Syt2 (cyan), and ChAT (magenta), respectively. Scale bar: 20 μm . (E) Intensity profiles of PKCa and Syt2 labeling from D relative to the location of the ChAT bands (magenta dotted lines). (F) The ending point of RBC terminal distribution (GCL side) was significantly closer to the ON-ChAT band (magenta dotted lines) in the *Trpm1* KO mouse retinas compared with the WT mouse retinas (starting point: WT: 116.3 \pm 4.2%, n = 3 sections from three mice; *Trpm1* KO: 113.3 \pm 9.5%, n = 3 sections from three mice; P = 0.65, ending point: WT: 222.1 \pm 3.8%, n = 3 sections from three mice; *Trpm1* KO: 195.4 \pm 6.7%, n = 3 sections from three mice; P = 0.0001). (G–I) Distribution of RBC terminals in the WT and *rd1* mouse retinas. (G) RBCs and SACs were immunolabeled with PKCa (green) and ChAT (magenta; IPL sublaminar marker), respectively. Scale bar: 20 μm . (H) WT *rd1*. (I) Relative position of RBC terminals in IPL (%). (J) Wild Type *rd1*. (K) Volume of RBC axon terminal (μm^3). (L–O) Marker expression for CA/mGluR6/GluK1 and PKCa/TRPM1. Panels L and M show CA/mGluR6/GluK1/DAPI and PKCa/TRPM1/DAPI expression in WT and *Trpm1* KO retinas, respectively. Panels N and O show CA/mGluR6/GluK1/DAPI and PKCa/TRPM1/DAPI expression in WT, *rd1*, and *mGluR6* KO retinas, respectively. White arrowheads in N and O indicate TRPM1 expression. Scale bars: 20 μm .

three mice; $P = 0.004$, unpaired t test). In contrast, the distribution of type 6 BC terminals was similar between WT and *Trpm1* KO mouse retinas (starting point: WT: $110.3 \pm 7.1\%$, $n = 3$ sections from three mice; *Trpm1* KO: $112.9 \pm 4.1\%$, $n = 3$ sections from three mice; $P = 0.62$, ending point: WT: $182.5 \pm 7.8\%$, $n = 3$ sections from three mice; *Trpm1* KO: $182.9 \pm 8.6\%$, $n = 3$ sections from three mice; $P = 0.96$, unpaired t test). (G–K) Altered distribution and reduced volume of RBC terminals in the *rd1* mouse retinas. (G–I) Distribution of RBC terminals was shifted toward the INL in the *rd1* mouse retinas. Similar analyses are shown in A–C (starting point: WT: $133.7 \pm 7.3\%$, $n = 5$ sections from five mice; *rd1*: $118.5 \pm 3.4\%$, $n = 5$ sections from five mice; $P = 0.003$, ending point: WT: $238.9 \pm 13.2\%$, $n = 5$ sections from five mice; *rd1*: $217.7 \pm 9.1\%$, $n = 5$ sections from five mice; $P = 0.02$). (J and K) Volume of RBC terminals in the *rd1* mouse retinas was smaller than that in the WT mouse retinas. (J) Synaptic terminals immunolabeled with PKCa (green) and VGLuT1 (magenta) in the WT (top) and *rd1* (bottom) mouse retinas. Scale bar: 5 μ m. (K) RBC terminal volumes were significantly smaller in the *rd1* mouse retinas than in the WT mouse retinas (WT: $5.7 \pm 5.7 \mu\text{m}^3$, $n = 107$ terminals, 3 retinas, 3 mice; *rd1*: $3.4 \pm 2.7 \mu\text{m}^3$, $n = 86$ terminals, 3 retinas, 3 mice; $P = 7.00 \times 10^{-4}$). (L–O) Marker expression in the OPL. (L) OPL localization of mGluR6 (green), CtBP2 (magenta), and DAPI (blue) was similar between WT (top) and *Trpm1* KO (bottom) mouse retinas. Scale bar: 5 μ m. (M) Cone pedicles remained intact in the *Trpm1* KO mouse retinas. Cone arrestin (yellow), mGluR6 (magenta), GluK1 (cyan), and DAPI (blue). Scale bar: 5 μ m. WT (top) and the *Trpm1* KO (bottom) mouse retinas. (N) TRPM1 puncta were moderately reduced in the *mGluR6* KO mouse retinas and severely diminished in the *rd1* mouse retinas. RBC dendrites showed intact structure in the *mGluR6* KO mouse retina but retracted in the *rd1* mouse retinas. WT (left), *rd1* (center), *mGluR6* KO (right) mouse retinas. Scale bar: 10 μ m. Insets show an enlarged view of individual RBC dendritic trees. Scale bar: 5 μ m. (O) Cone pedicles showed degeneration in the *rd1* mouse retinas. Cone arrestin (yellow), mGluR6 (magenta), GluK1 (cyan), and DAPI (blue). Scale bar: 5 μ m. WT (top) and *rd1* (bottom) mouse retinas. Data are presented as the mean \pm SD. Error bars indicate SD. n.s., not significant; * $P < 0.05$; ** $P < 0.01$; *** $P < 0.001$. SACs, starburst ACs.

hyperpolarization (Lagali et al., 2008; Koike et al., 2009). Since ON CBCs express T-type Ca^{2+} channels (de la Villa et al., 1998; Pan, 2000; Zhang et al., 2022), we hypothesized that these channels might allow glutamate release even at hyperpolarized membrane potentials. This condition was reproduced in those specific models by lowering the half-activation voltage of Ca^{2+} channels (see V_{th} in Eq. 5 in Materials and methods and additional details in the supplemental text at the end of the PDF) in the ON CBC terminals.

Using these retinal circuit models, we simulated the membrane potential changes of each cell. In the WT circuit model, all cell types (RBCs, OFF and ON CBCs, AII ACs, and OFF and ON RGCs) responded to light stimulation, and no membrane oscillations were observed (Fig. 5, A and B).

In the *Trpm1* KO circuit model (Fig. 5, C and D), RBCs were hyperpolarized and showed no ON response. OFF CBCs exhibited weak membrane oscillations and a hyperpolarizing light response. ON CBCs and AII ACs were hyperpolarized due to reduced inputs from RBCs to AII ACs and displayed membrane oscillations without ON responses. Both OFF and ON RGCs showed oscillatory firing, but only OFF RGCs responded to light stimulation.

In the *mGluR6* KO circuit model (Fig. 5, E and F), RBCs were hyperpolarized and lacked ON responses. OFF CBCs exhibited OFF responses to light stimulation but no obvious membrane oscillations. ON CBCs and AII ACs showed neither ON responses nor membrane oscillations. OFF and ON RGCs exhibited spontaneous firing, but only OFF RGCs responded to light stimulation. Such firing is unlikely to represent true oscillations, as they were not synchronized with fast membrane fluctuations of AII ACs. Rather, they may reflect intrinsic membrane properties of RGCs, which were not observed in our physiological recordings under the whole-cell voltage-clamp condition.

Notably, the circuit model reproduced RGC oscillations only in the *Trpm1* KO circuit model but not in the *mGluR6* KO circuit model. The critical difference between *Trpm1* KO and *mGluR6* KO circuit models is in the synaptic conductance from RBCs to AII ACs. In the *Trpm1* KO circuit model, this conductance was reduced to 0 due to axon terminal shrinkage, whereas it remained normal in the *mGluR6* KO circuit model, comparable to the WT levels. These findings suggest that reducing RBC-to-AII AC synaptic conductance may be essential for inducing membrane oscillations

in AII ACs. Supporting this conclusion, the *rd1* circuit model, which also included reduced synaptic conductance from RBCs to AII ACs, reproduced membrane oscillations (Fig. 5, G and H).

Reduced RBC synaptic input and ON CBC hyperpolarization drive AII AC oscillations

To evaluate how the membrane potential of RBC and ON CBC influences AII AC oscillations, we systematically manipulated parameters of the *Trpm1* KO circuit model. Although our original *Trpm1* KO circuit model exhibited membrane oscillations in AII ACs (Fig. 5 C), these oscillations disappeared when the synaptic conductance from RBC to AII AC ($g_{\text{RBC to AII AC}}$) was set to 1.0 (a value comparable to the WT circuit model) and the membrane potential of RBC and ON CBC was set to -68 and -52 mV, respectively (Fig. 6 A₁). In contrast, marked membrane oscillations were observed in AII ACs when the ON CBC membrane potential was hyperpolarized to -58 mV, while the RBC membrane potential and $g_{\text{RBC to AII AC}}$ were kept at -68 mV and 1.0, respectively (Fig. 6 A₂). Furthermore, marked membrane oscillations were also observed in AII ACs when $g_{\text{RBC to AII AC}}$ was reduced to 0.1, while the membrane potential of RBC and ON CBC remained the same (RBC: -68 mV, ON CBC: -52 mV; Fig. 6 A₃). A summary of the effects of the membrane potential of RBC and ON CBC on the AII AC activity is shown in Fig. 6 B. These simulations suggest that the membrane potential of ON CBC may play a more critical role in generating AII AC oscillations than that of RBC (Fig. 6, A₁ and A₂). Moreover, reducing the synaptic conductance from RBC to AII AC also had a significant impact on generating AII AC oscillations (Fig. 6, A₁ and A₃). Taken together, these results suggest that both reduction of the synaptic conductance from RBC to AII AC and hyperpolarization of ON CBC are key factors for generating AII AC oscillations.

Simulation of blocker effects on RGC firing

Using the *Trpm1* KO circuit model, we simulated the effects of pharmacological blockers by selectively modifying the relevant synaptic or gap junctional conductance. First, to mimic the effect of a glycine receptor antagonist, we set g_{glycine} to 0 nS. This manipulation eliminated inhibitory input from AII AC to OFF RGC (Fig. 7 A₃), resulting in tonic excitatory input from OFF CBC to OFF RGC (Fig. 7 A₂). Consequently, this tonic excitatory input but not periodic input evoked continuous firing in OFF RGC

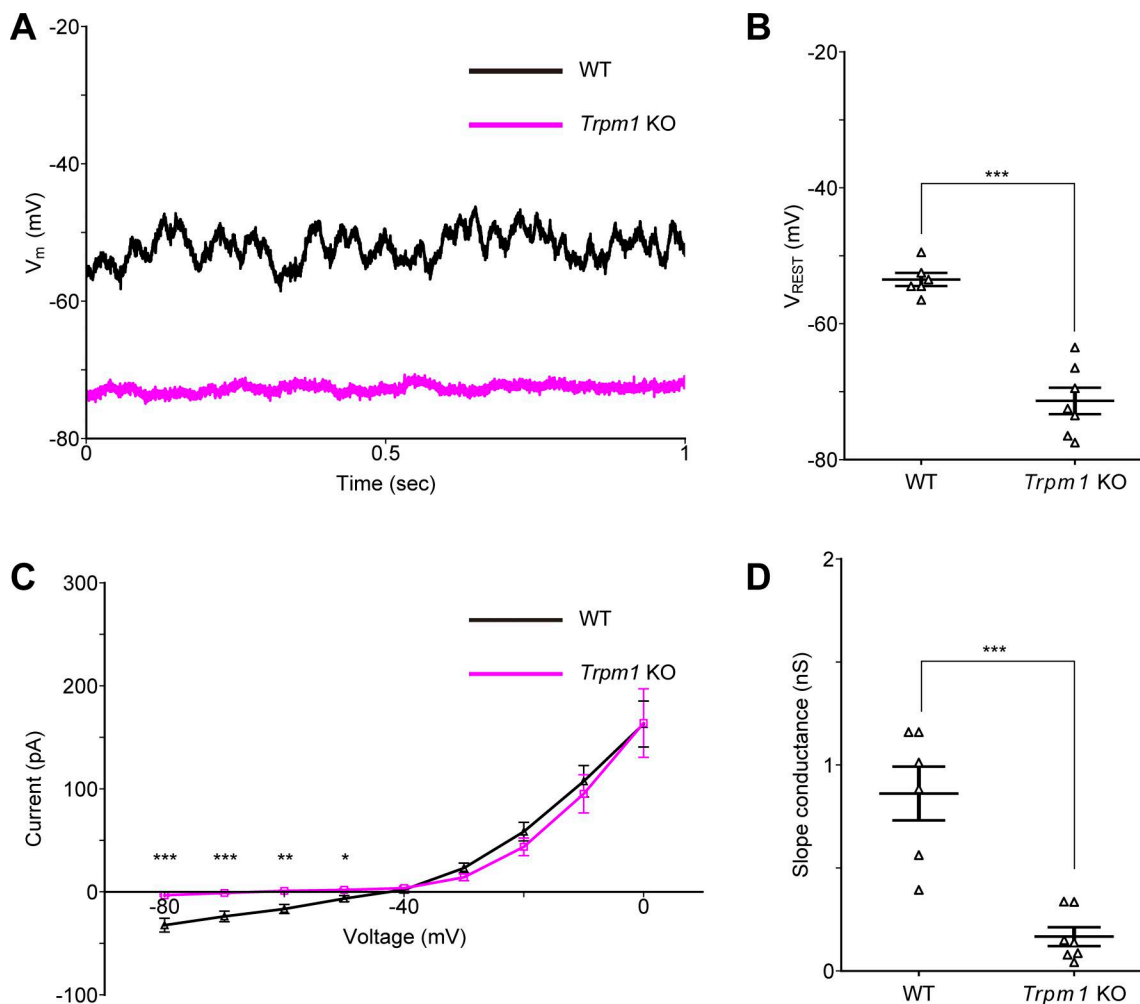


Figure 4. Resting membrane potential of RBCs in WT and *Trpm1* KO mouse retinas. **(A)** RBC membrane potential traces recorded from the WT (black) and *Trpm1* KO (magenta) mouse retinas. **(B)** Resting membrane potential of RBCs in the WT and *Trpm1* KO mouse retinas (WT: -53.5 ± 1.0 mV, $n = 6$ cells from five mice; *Trpm1* KO: -71.4 ± 1.9 mV, $n = 7$ cells from six mice; $P = 8.4 \times 10^{-6}$). **(C)** Averaged I-V curves of RBCs in WT (triangle, black, $n = 6$ cells from five mice) and *Trpm1* KO (square, magenta, $n = 7$ cells from six mice) mouse retinas. -80 mV: $P = 0.0007$; -70 mV: $P = 0.0007$; -60 mV: $P = 0.001$; -50 mV: $P = 0.02$. **(D)** Slope conductance of RBCs in the WT and *Trpm1* KO mouse retinas (WT: 0.86 ± 0.13 nS, $n = 6$ cells from five mice; *Trpm1* KO: 0.17 ± 0.05 nS, $n = 7$ cells from six mice; $P = 0.0002$). Data are presented as the mean \pm SEM. An unpaired *t* test was used for statistical analysis. n.s., not significant; * $P < 0.05$; ** $P < 0.01$; *** $P < 0.001$.

during the epoch without light stimulation (Fig. 7 A₁). OFF RGCs themselves or other GABAergic ACs may contribute to OFF RGC continuous firing. In response to light stimulation, OFF CBC reduced the excitatory input to OFF RGC (Fig. 7 A₂), resulting in an OFF response (Fig. 7 A₁). Notably, this parameter change did not affect the ON pathway (Fig. 7, A₄ and A₅).

Second, the effects of iGluR antagonist were mimicked by setting g_{iGluR} to 0 nS. Under this condition, oscillations in both OFF and ON RGCs disappeared (Fig. 7, B₁ and B₄). Excitatory inputs were eliminated from OFF CBC to OFF RGC (Fig. 7 B₂) and from ON CBC to ON RGC (Fig. 7 B₅), although inhibitory inputs from AII AC to OFF RGC were maintained (Fig. 7 B₃).

Finally, to mimic the effects of gap junction blockers, we set $g_{gap\ junction}$ to 0 nS. This manipulation reduced membrane oscillations in AII AC (Fig. 7 C₃) and rendered inhibitory inputs from AII AC to OFF CBC and OFF RGC tonic (Fig. 7, C₂ and C₃). This resulted in reduced periodicity of OFF RGCs (Fig. 7 C₁). Furthermore, membrane oscillations in both ON CBC and AII AC

disappeared, and tonic excitatory inputs from ON CBC to ON RGC (Fig. 7 C₅) led to repetitive firing (Fig. 7 C₄). These simulations demonstrate that our *Trpm1* KO circuit model successfully reproduced the blocker effects comparable to our electrophysiological results (Fig. 2).

Discussion

In animal models of RP, including the *rd1* mouse, severe malformations in the inner retina complicate our understanding of the mechanisms underlying pathological RGC oscillations. However, the *Trpm1* KO mouse retina, which retains intact photoreceptors, also displays pathological RGC oscillations. Thus, the *Trpm1* KO mouse retina provides a valuable system for investigating the mechanisms of RGC oscillations in a structurally less compromised context.

In the present study, we investigated the mechanisms underlying RGC oscillations in the *Trpm1* KO mouse retina. We

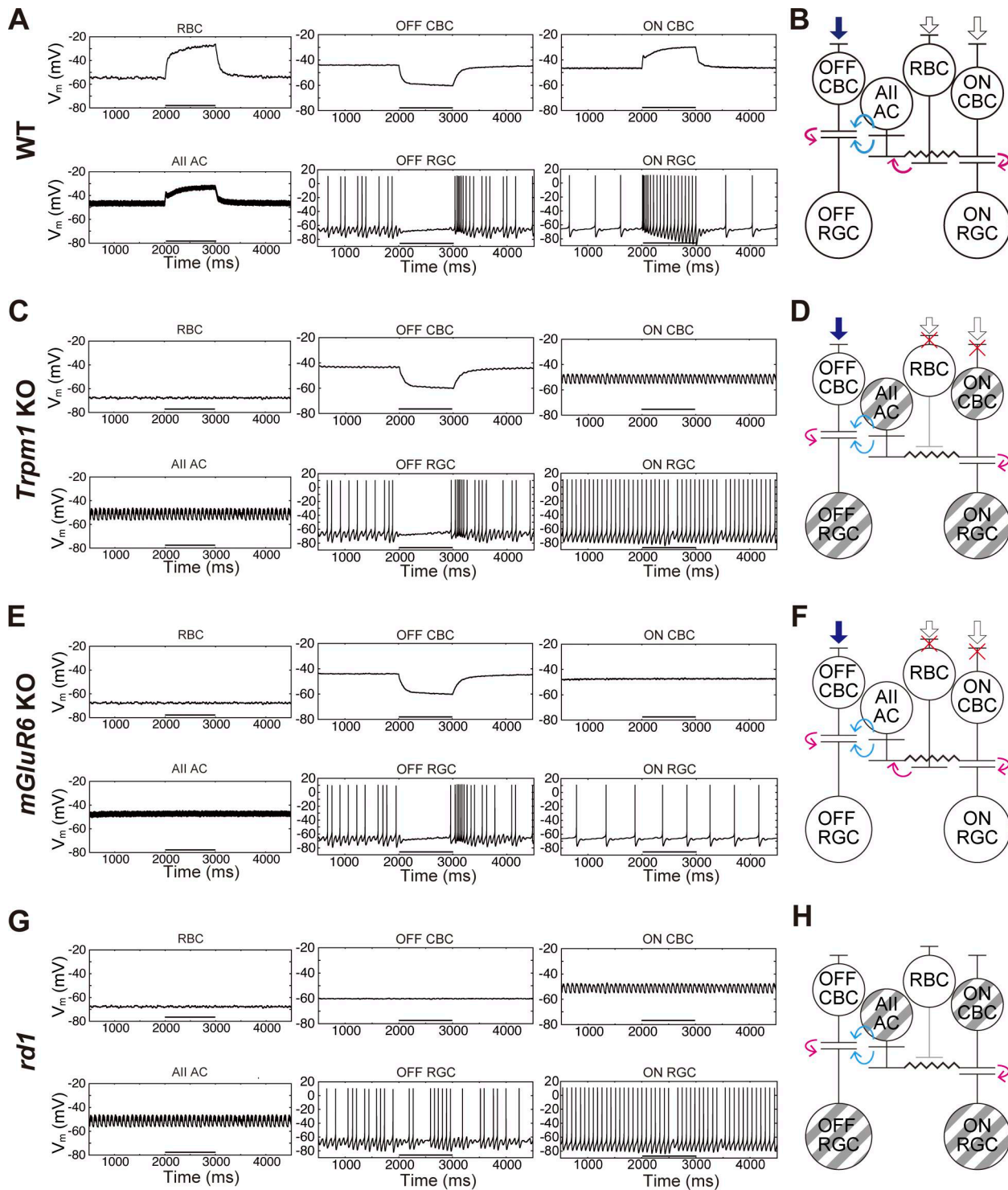


Figure 5. Numerical simulation of retinal neural circuit models. **(A)** Simulated membrane potential changes in RBCs, OFF CBCs, ON CBCs, All ACs, OFF RGCs, and ON RGCs in the WT circuit model. Light stimulation (black bar: bottom) hyperpolarizes OFF CBCs, while it depolarizes RBCs, ON CBCs, and All ACs. The firing rate increases at light offset in OFF RGCs and at light onset in ON RGCs. **(B)** Schematic diagram of the WT circuit model. Filled and open arrows to BCs indicate hyperpolarizing and depolarizing current inputs, respectively. Excitatory (magenta) and inhibitory (cyan) synapses, as well as gap junctions (—), are illustrated. **(C)** Simulated membrane potential changes in the *Trpm1* KO circuit model. OFF CBCs and OFF RGCs respond to light stimulation. RBCs, ON CBCs, All ACs, and ON RGCs show no light responses due to the loss of TRPM1. ON CBCs and All ACs exhibit membrane oscillations. Both OFF and ON RGCs show spontaneous oscillatory firing. **(D)** Schematic diagram of the *Trpm1* KO circuit model. Due to the loss of TRPM1, RBCs and ON CBCs do not respond to light stimulation. The cells with oscillations are shown by striped patterns. **(E)** Simulated membrane potential changes in the *mGluR6* KO circuit model. OFF CBCs and OFF RGCs respond to light stimulation. RBCs, ON CBCs, All ACs, and ON RGCs show no light responses due to the loss of mGluR6. ON CBCs and All ACs do not exhibit marked membrane oscillations. **(F)** Schematic diagram of the *mGluR6* KO circuit model. Due to the loss of mGluR6, RBCs and ON CBCs do not respond to light stimulation. **(G)** Simulated membrane potential changes in the *rd1* circuit model. RBCs, ON CBCs, OFF CBCs, All ACs, OFF RGCs, and ON RGCs show no light

responses due to photoreceptor degeneration. ON CBCs and AII ACs exhibit membrane oscillations, similar to those observed in the *Trpm1* KO circuit model (C). OFF and ON RGCs show spontaneous oscillatory firing. (H) Schematic diagram of the *rd1* circuit model. Due to photoreceptor degeneration, BCs do not receive synaptic currents from photoreceptors. The cells with oscillations are shown by striped patterns.

found that the RGC oscillations in OFF αRGCs are driven by inhibitory inputs mediated by glycine receptors, while oscillations in ON αRGCs arise from excitatory inputs mediated by glutamate receptors (Figs. 1 and 2). Notably, a gap junction blocker eliminated oscillations in both RGC types, suggesting a common upstream origin within an electrically coupled network (Fig. 2). Furthermore, *Trpm1* KO mouse retina displayed morphological alterations in RBCs, similar to the *rd1* mouse retina (Fig. 3). The membrane potential of RBCs in the *Trpm1* KO mouse retina was significantly hyperpolarized (Fig. 4). Finally, our mathematical modeling reproduced the RGC oscillations by incorporating these structural changes and the loss of ON signals, suggesting that TRPM1 loss, hyperpolarization, and axon shortening are precursors to oscillations in the AII AC network (Figs. 5 and 6).

Mechanisms of RGC oscillations in the *Trpm1* KO mouse retina

Computer simulations suggest that RGC oscillations in the *Trpm1* KO mouse retina arise from reducing inputs from RBC and ON

CBC to AII AC (Figs. 5 and 6). This reduction may be ascribed to shrinkage of RBC axon terminals, which may be caused by the loss of TRPM1 localization at the dendritic tips of RBCs (Fig. 3 N) (Kozuka et al., 2017; Takeuchi et al., 2018). Such smaller RBC axon terminals may impair the functionality of the release machinery, for instance, through a reduction of Ca^{2+} channels and/or a decreased number of ribbons and synaptic vesicles. Therefore, future detailed experiments focusing on the synaptic transmission from BCs (particularly RBCs) to AII ACs are warranted.

Furthermore, the loss of TRPM1 localization at the dendritic tips of ON BCs may lead to their hyperpolarization. Indeed, our data show that the resting membrane potential of RBCs in the *Trpm1* KO mouse retinas is more hyperpolarized than that in the WT mouse retinas (Fig. 4). This result suggests that ON CBCs may also be hyperpolarized in the *Trpm1* KO mouse retina. These changes could, in turn, contribute to a modest hyperpolarization and membrane oscillations of AII ACs.

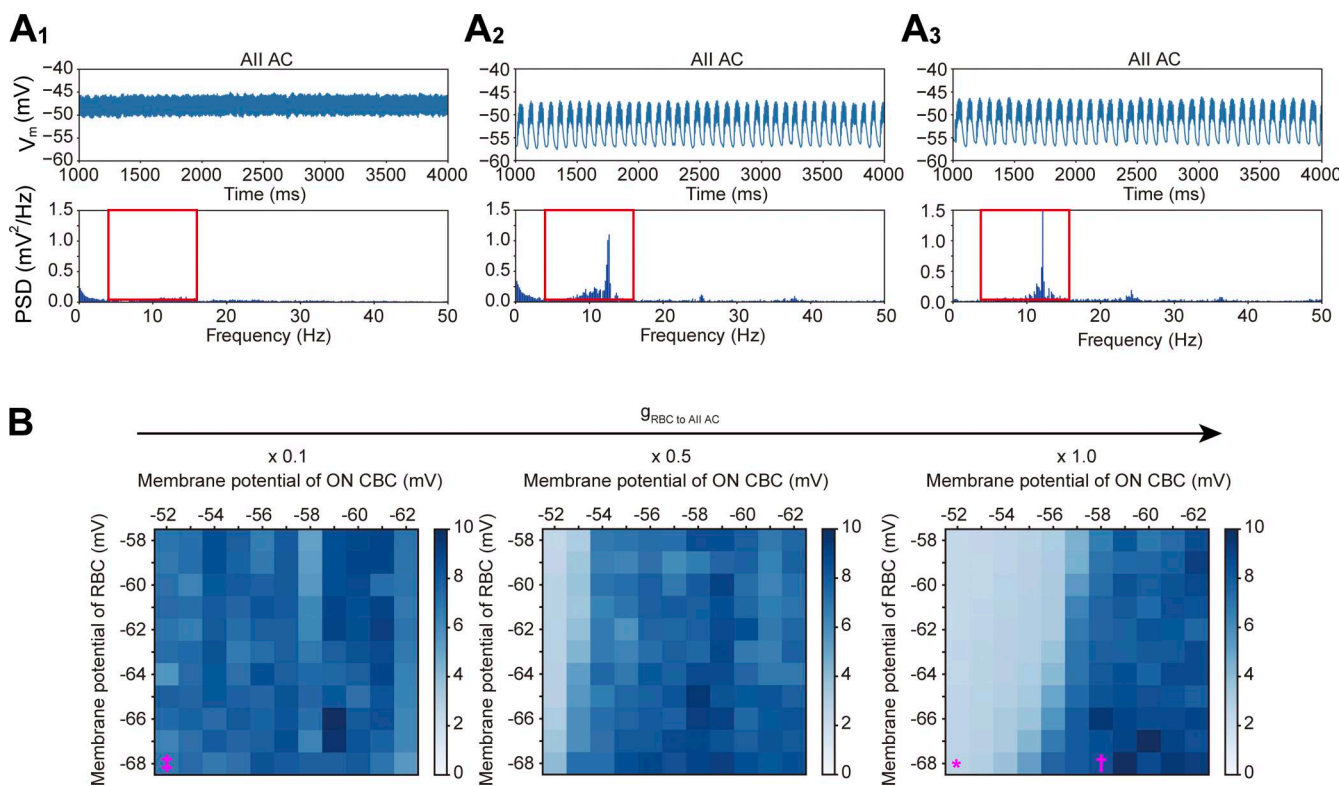


Figure 6. Dependence of AII AC oscillations on RBC-to-AII AC synaptic conductance and ON CBC membrane potential. (A) Representative simulation results under three different conditions (A₁–A₃). In each panel, the top trace shows the simulated AII AC membrane potential, and the bottom plot shows the corresponding PSD. The red square in PSD indicates the 5–15 Hz ROI used for analysis. (A₁) Simulation with the membrane potential of -68 mV for RBC and -52 mV for ON CBC, and a $g_{\text{RBC to AII AC}}$ of 1.0 (comparable to WT). (A₂) Simulation with the ON CBC membrane potential hyperpolarized to -58 mV. Other parameters are the same as in A₁. (A₃) Simulation with $g_{\text{RBC to AII AC}}$ reduced to 0.1. Other parameters are the same as in A₁. (B) Summary of the relationship between the strength of AII AC oscillations and the membrane potential of RBC and ON CBC. The synaptic conductance from RBC to AII AC was changed. The symbols indicate the simulated conditions shown in A₁ (*), A₂ (†), and A₃ (‡). Color intensity represents the integrated value of the PSD calculated from the ROI.

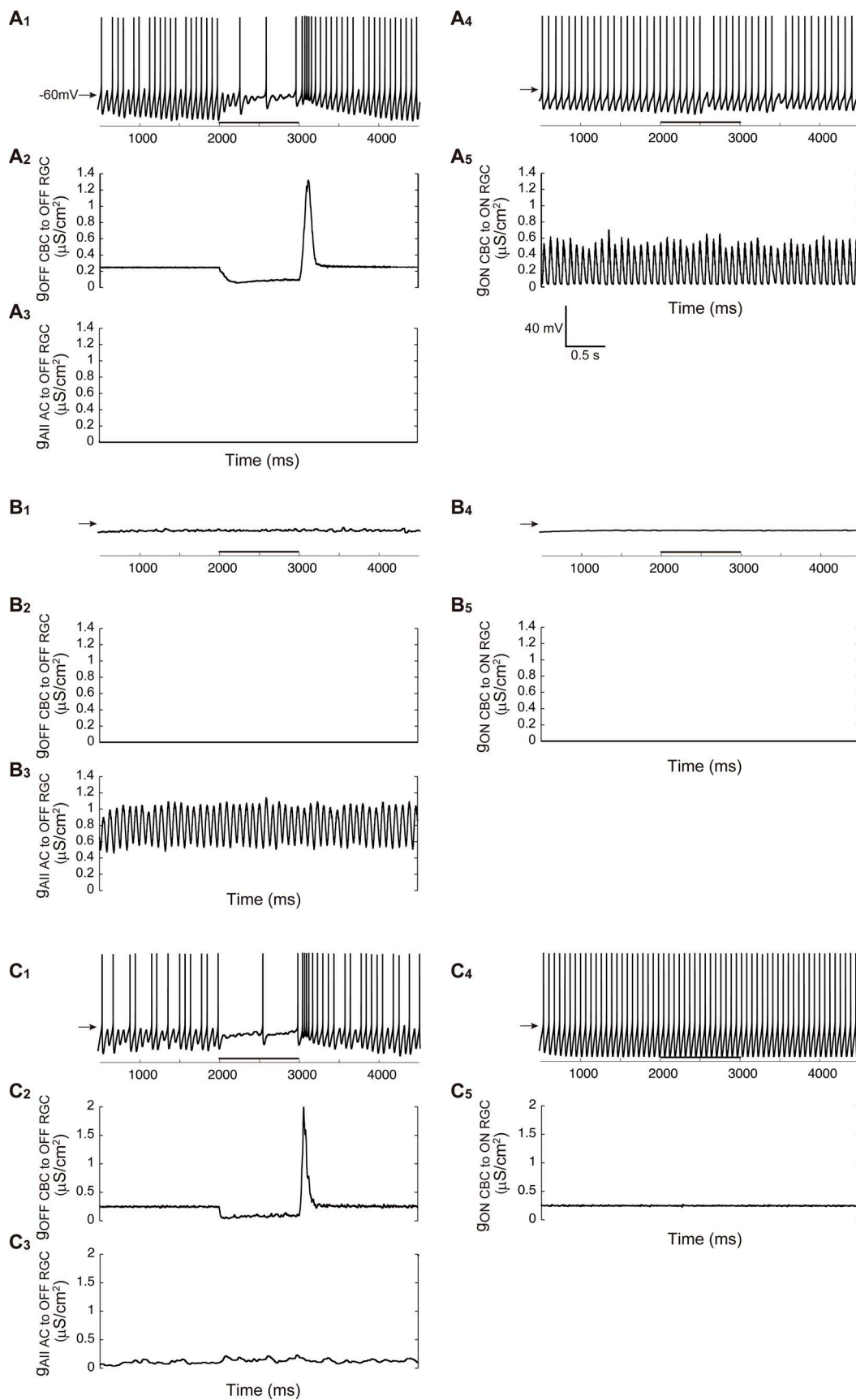


Figure 7. Simulation of pharmacological blockade in the *Trpm1* KO circuit model. **(A₁-A₅)** Simulated blockade of glycinergic synaptic transmission. Each panel shows the membrane potential change in OFF RGC (A₁), synaptic conductance from OFF CBC to OFF RGC (A₂), synaptic conductance from All AC to OFF

RGC (A_3), membrane potential change in ON RGC (A_4), and synaptic conductance from ON CBC to ON RGC (A_5). Horizontal bars indicate light stimulation. **(B₁-B₅)** Simulated blockade of glutamatergic synaptic transmission. Panel arrangement is as in A. **(C₁-C₅)** Simulated blockade of gap junctions. Panel arrangement is as A and B.

Comparison between *Trpm1* KO and *mGluR6* KO mouse retinas

The *Trpm1* KO mouse retina exhibits prominent spontaneous RGC oscillations. In contrast, *mGluR6*-mutant mice, one of CSNB models, exhibit infrequent or absent RGC oscillations (Renteria et al., 2006; Takeuchi et al., 2018; Hasan et al., 2020; Hölzel et al., 2023). For instance, Hasan et al. (2020) found that only ~4% of RGCs in *mGluR6* KO mice oscillate in darkness. Hölzel et al. (2023) also reported that oscillatory activity can be evoked by light stimulation in a small proportion of RGCs (~5%), but absent oscillations are observed in the dark. These infrequent or stimulus-dependent oscillations differ markedly from the robust and spontaneous oscillations observed in *Trpm1* KO mouse retinas, where ~50% of RGCs exhibit oscillatory activity even in the absence of light stimulation (Takeuchi et al., 2018).

In addition to functional differences, the *mGluR6* KO retina also exhibits distinct morphological features compared with the *Trpm1* KO mouse retina. For example, TRPM1 localization at the ON BC dendritic tips is reduced but still detectable in the *mGluR6* KO mouse retinas (Fig. 3 N) (Xu et al., 2012), and the distribution and size of RBC axon terminals are comparable to those in WT mouse retinas (Fig. 3, A-C) (Kozuka et al., 2017; Takeuchi et al., 2018). These observations suggest that the synaptic transmission from RBC to AII AC may be relatively unimpaired in the *mGluR6* KO mouse retina.

Although the loss of *mGluR6* is theoretically expected to render TRPM1 channels constitutively open, RBCs in both *Trpm1* KO (Fig. 4, A and B) and *mGluR6* KO mouse retinas are hyperpolarized (Xu et al., 2012). We measured a 0.20 ratio between the slope conductance in the voltage range around the resting membrane potential in the *Trpm1* KO and WT, consistent with a marked reduction in membrane conductance (*Trpm1* KO: 0.17 ± 0.05 nS; WT: 0.86 ± 0.13 nS) (Fig. 4 D). In comparison, Xu et al. (2012) found a ratio of 0.59 for *mGluR6* KO versus WT mice under similar recording conditions (*mGluR6* KO: 1.09 ± 0.08 nS; WT: 1.84 ± 0.26 nS). This difference suggests that the residual TRPM1 channels at the dendritic tips of RBCs in the *mGluR6* KO mouse retina may remain functional and exhibit spontaneous gating. This preserved channel activity may contribute to the structural maturation of RBCs in the *mGluR6* KO mouse retina, thereby explaining their near-normal morphology and a lack of robust network oscillations.

Comparison between *Trpm1* KO and *rdl* mouse retinas

The neural oscillations in the *Trpm1* KO mouse retina revealed in this study share striking similarities to the phenomenon reported in the *rdl* mouse retina. This suggests that despite their distinct genetic backgrounds, both mouse retinas form a functionally equivalent pathological oscillatory network.

The fundamental physiological characteristics of the oscillations are almost identical in both mouse models. The oscillation frequency determined from the extracellular potential of RGCs was ~8 Hz in the *Trpm1* KO mouse retina (Takeuchi et al.,

2018), which is comparable to the ~9 Hz in the *rdl* mouse retina (Menzler and Zeck, 2011). Furthermore, the phase relationships of oscillations between αRGCs (anti-phase between different-type cell pairs, in-phase between same-type cell pairs) and the pattern of synaptic inputs, in which OFF αRGCs receive oscillatory inhibitory inputs and ON αRGCs receive excitatory inputs (Fig. 1), were in agreement with reports from the *rdl* mouse retina (Margolis et al., 2008, 2014). This convergence of multiple physiological features strongly suggests that a common underlying circuit is in operation.

These functional similarities appear to stem from shared functional and morphological alterations in RBCs. Although RBCs in the *rdl* mouse retina were predicted to be depolarized due to a decrease in *mGluR6* (Strettoi and Pignatelli, 2000; Strettoi et al., 2002, 2003), direct recordings have shown that they are hyperpolarized (Borowska et al., 2011), similar to the *Trpm1* KO mouse retina (Fig. 4). This phenomenon is consistent with the marked reduction of TRPM1 at the dendritic tips of RBCs in the *rdl* mouse retina (Fig. 3 N) and aligns with previous reports establishing a link between TRPM1 reduction and RBC hyperpolarization (Ou et al., 2015). Moreover, our study reveals that RBCs in *Trpm1* KO and *rdl* mouse retinas share morphological alterations, including reduced TRPM1 localization at dendritic tips, changes in axonal terminal distribution, and shrinkage of axonal terminals (Fig. 3) (Takeuchi et al., 2018). These shared pathologies likely serve as a critical trigger for driving the downstream oscillatory network.

Taken together, the multiple commonalities, including the oscillation frequency, phase relationships, synaptic input patterns, and the upstream hyperpolarization and morphological alterations in RBCs, strongly support the view that the oscillations in the *Trpm1* KO and *rdl* retinas are essentially equivalent phenomena driven by a common circuit mechanism.

Retinal oscillations in CSNB and *rd* mouse retinas

Trpm1 is one of the genes responsible for CSNB (Nakamura et al., 2010). Other genes implicated in CSNB include *mGluR6* and *Ca_v1.4*. Additionally, genes such as *Nyx* and *Lrit3*, which encode proteins essential for the correct localization of TRPM1 to the dendritic tips of ON BCs, are also associated with CSNB (Pearring et al., 2011; Neuillé et al., 2015; Zeitz et al., 2015). With the notable exception of the *mGluR6* KO mouse retinas, which retain TRPM1, spontaneous RGC oscillations comparable to those in the *Trpm1* KO mouse retinas have been described in the *Nyx^{nob}*, *Ca_v1.4* KO, and *Lrit3^{emrggl}* mouse retinas (Winkelman et al., 2019; Hasan et al., 2020; Hölzel et al., 2023). RGC oscillations have also been reported in the *rdl10* mouse retinas (Goo et al., 2011; Toychiev et al., 2013), other RP model mice. Immunohistochemical investigation, including our findings for the *Trpm1* KO and *rdl* mouse retinas, has revealed that TRPM1 localization is absent or reduced at the dendritic tips of ON BCs in the oscillated retinas, such as *Trpm1* KO, *Nyx^{nob}*, *Lrit3^{emrggl}*, *Ca_v1.4* KO, *rdl*, and *rdl10*.

Table 2. Summary of pathological oscillations and TRPM1 localization in the CSNB and *rd* mouse retinas

Mutant name	Pathological oscillations	Localization of TRPM1	Disease
<i>Trpm1</i> KO	Yes, Fig. 1; Takeuchi et al., 2018	Absent, Koike et al., 2009; Morgans et al., 2009	CSNB
<i>mGluR6</i> KO	Nearly absent, Takeuchi et al., 2018 Infrequent, Hasan et al., 2020	Slightly weak, Fig. 3 N; Xu et al., 2012	CSNB
<i>Nyx</i> ^{nob3}	Yes, Winkelman et al., 2019; Hözel et al., 2023	Absent, Pearring et al., 2011	CSNB
<i>Lrit3</i> ^{emrgg1}	Yes, Hasan et al., 2020	Absent, Hasan et al., 2019	CSNB
<i>Ca_v1.4</i> KO	Yes, Hözel et al., 2023	Reduced and/or absent, Maddox et al., 2020	CSNB
<i>rd1</i>	Yes, Margolis et al., 2008; Margolis et al., 2014; Stasheff, 2008; Borowska et al., 2011; Menzler and Zeck, 2011; Yee et al., 2012; Choi et al., 2014; Poria and Dhingra, 2015	Reduced, Fig. 3 N; Križaj et al., 2010	RP
<i>rd10</i>	Yes, Goo et al., 2011; Toychiev et al., 2013	Absent, Gayet-Primo and Puthussery, 2015	RP

mouse retinas (Fig. 3 N and Table 2) (Koike et al., 2009; Morgans et al., 2009; Križaj et al., 2010; Pearring et al., 2011; Gayet-Primo and Puthussery, 2015; Hasan et al., 2019; Maddox et al., 2020). The *rd1* and *rd10* mice are models of RP that cause photoreceptor degeneration but relatively preserve BCs. This raises the question of why the *rd* retina loses TRPM1 from the dendritic tips of ON BCs despite no direct genetic defect in TRPM1 itself. As Hasan et al. (2019) have shown that LRIT3 is necessary for the localization of TRPM1 to the dendritic membrane of ON BCs and is located at photoreceptor terminals, it is plausible that the extent of photoreceptor degeneration affects LRIT3 expression and/or localization, which may influence the degree of TRPM1 loss at the dendritic tips of RBCs. Collectively, our results suggest that the loss of TRPM1 localization at RBC dendritic tips may precede and contribute to the observed alterations in RBC axon terminal distribution and shrinkage. Therefore, TRPM1 loss could also contribute to RGC oscillations in the *rd* mouse retinas.

In the degenerating *rd10* mouse retina, it is reported that the membrane potential of RBCs is depolarized when some rod photoreceptors still survive (Li et al., 2024, Preprint), suggesting that some TRPM1 channels may remain functional in RBC dendrites during this stage. However, after complete rod photoreceptor degeneration in the *rd10* mouse retina, TRPM1 localization at RBC dendrites is absent. Furthermore, RGC oscillations have also been observed at this stage of degeneration (Goo et al., 2011; Gayet-Primo and Puthussery, 2015). Our proposed mechanism involving TRPM1 loss at RBC dendritic tips as a driver of pathological oscillations may also explain the oscillations observed in the late stage of degeneration in the *rd10* mouse.

It has been reported that the retinoic acid (RA) level increases in the *rd* mouse retinas due to photoreceptor degeneration, which, in turn, contributes to RGC hyperactivity (Telias et al., 2019, 2022). Given that the outer retinal layers remain intact in the *Trpm1* KO retina, it is unlikely that RA levels are elevated in this model. In our present study, we identified common morphological alterations in RBCs from both *Trpm1* KO and *rd1* mouse retinas, including altered terminal distribution in the IPL, reduced axon terminal size, and loss of TRPM1 at dendritic tips. The absence or reduction of TRPM1 localization at RBC dendritic tips is a consistent feature across oscillating retinas, including those in RP models and certain CSNB models. Taken together, these results suggest that the loss of TRPM1 at the dendritic tips of ON BCs could be a significant contributor to RGC oscillations, potentially independent of RA signaling.

Comparison between computational models

Several models have been proposed to account for spontaneous oscillatory activity in the mouse retina, including models for *rd1* retina (Ly et al., 2022) and for CSNB retina (Hözel et al., 2023). These models, as well as our model, share the common mechanism based on the properties of AII ACs reported by Choi et al. (2014). Fig. 8 presents a conceptual framework that synthesizes our interpretation of experimental results under various conditions (Fig. 2 in this paper; Trenholm et al., 2012; Choi et al., 2014; Takeuchi et al., 2018), illustrating the proposed relationship between the level of AII AC membrane potential and contributing inputs to AII AC. AII AC exhibits three distinct activity modes: high-frequency fluctuations caused by abundant sodium channels at the initiation site in the depolarized state (Fig. 8, zone A), low-frequency (~10 Hz) and large-amplitude oscillations in the intermediate range of membrane potential (Fig. 8, zone B), and no oscillations due to sodium channel inactivation in the hyperpolarized state (Fig. 8, zone C). Since the low-frequency oscillations in the intermediate range (zone B) are regarded as the source of spontaneous oscillatory activity observed in degenerated retinas, and since the membrane potential of AII AC in the WT mouse retina is more depolarized than that in the *rd1* mouse retina (Choi et al., 2014), AII ACs in the WT mouse retina are presumed to stay in the depolarized state (zone A). Therefore, AII ACs are thought to receive depolarizing inputs from other cell types, and a reduction in these inputs can cause oscillations in AII ACs, leading to spontaneous RGC oscillations. The assumptions of these models are primarily different in regard to the inputs to AII AC. Although other (or previous) models assumed only the gap junctional input from ON CBC to AII AC, our present model considers excitatory inputs from RBCs to AII ACs in addition to the gap junctional input. Considering two excitatory inputs to AII AC enables us to understand physiological results more consistently.

In conclusion, our study suggests a final common mechanism for pathological retinal oscillations, applicable to conditions ranging from severe degeneration to specific genetic alterations like the *Trpm1* KO. This relatively simple model, capable of producing a full range of oscillatory behaviors, provides a robust framework for future investigations into secondary dysfunctions, such as pathological RGC oscillations in various retinal diseases.

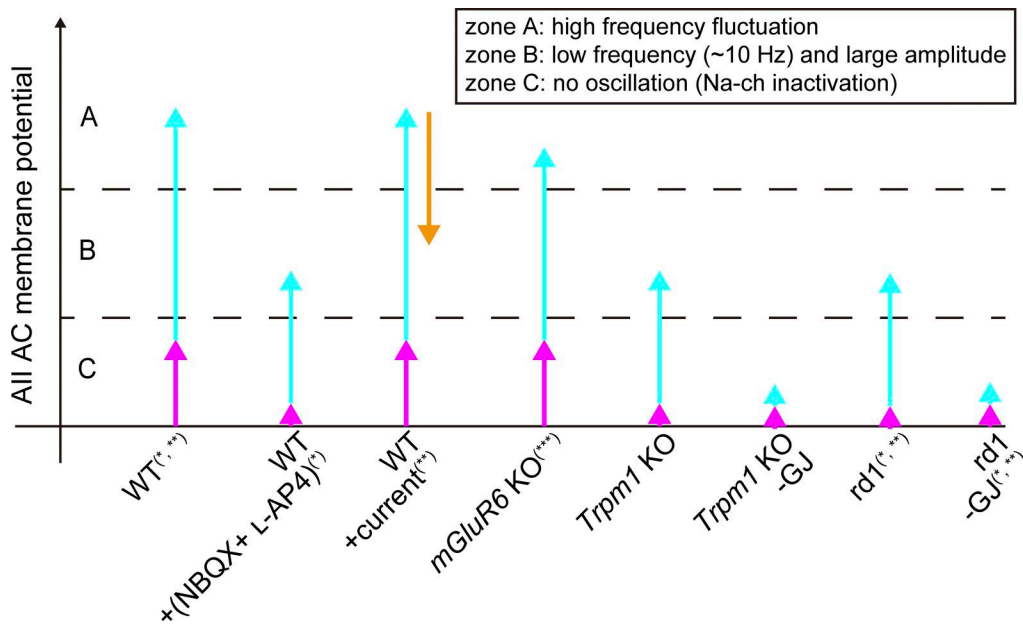


Figure 8. Relationship between All AC input and All AC oscillation. The All AC receives excitatory inputs from two primary sources: RBC (magenta) and ON CBC via gap junction (cyan). The orange arrow represents an applied current. GJ, gap junction. The symbols correspond to the following references: *, Trenholm et al., 2012; **, Choi et al., 2014; **, Takeuchi et al., 2018.

Data availability

The data that support the findings of this study are available from the corresponding author upon reasonable request.

Acknowledgments

Christopher J. Lingle served as editor.

We thank Drs. Takahisa Furukawa and Shigetada Nakanishi for the *Trpm1* KO and *mGluR6* KO mice, respectively, and Dr. Michiko Mandai for the *rd1* mouse retina. We also thank Dr. Kirill A. Martemyanov, University of Florida, Gainesville, FL, USA for TRPM1 antibody.

This work was supported by Japan Society for the Promotion of Science Grants-in-Aid for Scientific Research Grants 24H00747, 22KK0137, 19H01140, and 24390019, Takeda Science Foundation, the Kobayashi Foundation, JST PRESTO, and R-GIRO.

Author contributions: Sho Horie: conceptualization, data curation, formal analysis, investigation, methodology, project administration, resources, software, validation, visualization, and writing—original draft, review, and editing. Konan Sakuta: formal analysis and investigation. Keigo Tada: data curation, formal analysis, investigation, and software. Haruki Tokumoto: formal analysis, investigation, visualization, and writing—review and editing. Taketo Nishimoto: data curation, investigation, and validation. Katsunori Kitano: data curation, formal analysis, funding acquisition, investigation, methodology, software, supervision, validation, visualization, and writing—original draft, review, and editing. Masao Tachibana: conceptualization, formal analysis, funding acquisition, investigation, methodology, project administration, resources, supervision, validation, visualization, and writing—original

draft, review, and editing. Chieko Koike: conceptualization, funding acquisition, project administration, resources, supervision, visualization, and writing—original draft, review, and editing.

Disclosures: The authors declare no competing interests exist.

Submitted: 26 December 2024

Revised: 22 July 2025

Revised: 16 August 2025

Accepted: 3 September 2025

References

Arai, I., M. Tanaka, and M. Tachibana. 2010. Active roles of electrically coupled bipolar cell network in the adult retina. *J. Neurosci.* 30: 9260–9270. <https://doi.org/10.1523/JNEUROSCI.1590-10.2010>

Arman, A.C., and A.P. Sampath. 2012. Dark-adapted response threshold of OFF ganglion cells is not set by OFF bipolar cells in the mouse retina. *J. Neurophysiol.* 107:2649–2659. <https://doi.org/10.1152/JN.01202.2011>

Baden, T., P. Berens, K. Franke, M. Román Rosón, M. Bethge, and T. Euler. 2016. The functional diversity of retinal ganglion cells in the mouse. *Nature*. 529:345–350. <https://doi.org/10.1038/nature16468>

Borowska, J., S. Trenholm, and G.B. Awatramani. 2011. An intrinsic neural oscillator in the degenerating mouse retina. *J. Neurosci.* 31:5000–5012. <https://doi.org/10.1523/JNEUROSCI.5800-10.2011>

Carter-Dawson, L.D., M.M. Lavail, and R.L. Sidman. 1978. Differential effect of the rd mutation on rods and cones in the mouse retina. *Invest. Ophthalmol. Vis. Sci.* 17:489–498.

Cembrowski, M.S., S.M. Logan, M. Tian, L. Jia, W. Li, W.L. Kath, H. Riecke, and J.H. Singer. 2012. The mechanisms of repetitive spike generation in an axonless retinal interneuron. *Cell Rep.* 1:155–166. <https://doi.org/10.1016/j.celrep.2011.12.006>

Chen, M., K. Wang, and B. Lin. 2012. Development and degeneration of cone bipolar cells are independent of cone photoreceptors in a mouse model of retinitis pigmentosa. *PLoS One.* 7:e44036. <https://doi.org/10.1371/JOURNAL.PONE.0044036>

Choi, H., L. Zhang, M.S. Cembrowski, C.F. Sabottke, A.L. Markowitz, D.A. Butts, W.L. Kath, J.H. Singer, and H. Riecke. 2014. Intrinsic bursting of

All amacrine cells underlies oscillations in the rd1 mouse retina. *J. Neurophysiol.* 112:1491–1504. <https://doi.org/10.1152/JN.00437.2014>

Chua, J., E.L. Fletcher, and M. Kalloniatis. 2009. Functional remodeling of glutamate receptors by inner retinal neurons occurs from an early stage of retinal degeneration. *J. Comp. Neurol.* 514:473–491. <https://doi.org/10.1002/CNE.22029>

de la Villa, P., C.F. Vaquero, and A. Kaneko. 1998. Two types of calcium currents of the mouse bipolar cells recorded in the retinal slice preparation. *Eur. J. Neurosci.* 10:317–323. <https://doi.org/10.1046/J.1460-9568.1998.00051.X>

Dunn, F.A., T. Doan, A.P. Sampath, and F. Rieke. 2006. Controlling the gain of rod-mediated signals in the mammalian retina. *J. Neurosci.* 26: 3959–3970. <https://doi.org/10.1523/JNEUROSCI.5148-05.2006>

Feigenspan, A., B. Teubner, K. Willecke, and R. Weiler. 2001. Expression of neuronal connexin36 in AII amacrine cells of the mammalian retina. *J. Neurosci.* 21:230–239. <https://doi.org/10.1523/JNEUROSCI.21-01-00230.2001>

Fohlmeister, J.F., E.D. Cohen, and E.A. Newman. 2010. Mechanisms and distribution of ion channels in retinal ganglion cells: Using temperature as an independent variable. *J. Neurophysiol.* 103:1357–1374. <https://doi.org/10.1152/JN.00123.2009>

Gayet-Primo, J., and T. Puthussery. 2015. Alterations in kainate receptor and TRPM1 localization in bipolar cells after retinal photoreceptor degeneration. *Front. Cell. Neurosci.* 9:486. <https://doi.org/10.3389/FNCEL.2015.00486>

Goo, Y.S., K.N. Ahn, Y.J. Song, S.H. Ahn, S.K. Han, S.B. Ryu, and K.H. Kim. 2011. Spontaneous oscillatory rhythm in retinal activities of two retinal degeneration (rd1 and rd10) mice. *Korean J. Physiol. Pharmacol.* 15: 415–422. <https://doi.org/10.4196/KJPP.2011.15.6.415>

Grabner, C.P., C.P. Ratliff, A.C. Light, and S.H. DeVries. 2016. Mechanism of high-frequency signaling at a depressing ribbon synapse. *Neuron.* 91: 133–145. <https://doi.org/10.1016/J.NEURON.2016.05.019>

Graydon, C.W., E.E. Lieberman, N. Rho, K.L. Briggman, J.H. Singer, and J.S. Diamond. 2018. Synaptic transfer between rod and cone pathways mediated by AII amacrine cells in the mouse retina. *Curr. Biol.* 28: 2739–2751.e3. <https://doi.org/10.1016/J.CUB.2018.06.063>

Grover, S., G.A. Fishman, R.J. Anderson, M.S. Tozatti, J.R. Heckenlively, R.G. Weleber, A.O. Edwards, and J. Brown. 1999. Visual acuity impairment in patients with retinitis pigmentosa at age 45 years or older. *Ophthalmology.* 106:1780–1785. [https://doi.org/10.1016/S0161-6420\(99\)90342-1](https://doi.org/10.1016/S0161-6420(99)90342-1)

Haq, W., B. Arango-Gonzalez, E. Zrenner, T. Euler, and T. Schubert. 2014. Synaptic remodeling generates synchronous oscillations in the degenerated outer mouse retina. *Front. Neural Circuits.* 8:108. <https://doi.org/10.3389/FNCIR.2014.00108>

Hartong, D.T., E.L. Berson, and T.P. Dryja. 2006. Retinitis pigmentosa. *Lancet.* 368:1795–1809. [https://doi.org/10.1016/S0140-6736\(06\)69740-7](https://doi.org/10.1016/S0140-6736(06)69740-7)

Hasan, N., G. Pangeni, C.A. Cobb, T.A. Ray, E.R. Nettesheim, K.J. Ertel, D.M. Lipinski, M.A. McCall, and R.G. Gregg. 2019. Presynaptic expression of LRIT3 transsynaptically organizes the postsynaptic glutamate signaling complex containing TRPM1. *Cell Rep.* 27:3107–3116.e3. <https://doi.org/10.1016/j.celrep.2019.05.056>

Hasan, N., G. Pangeni, T.A. Ray, K.M. Fransen, J. Noel, B.G. Borghuis, M.A. McCall, and R.G. Gregg. 2020. LRIT3 is required for nyctalopin expression and normal ON and OFF Pathway signaling in the retina. *eNeuro.* 7:ENEURO.0002-20.2020. <https://doi.org/10.1523/ENEURO.0002-20.2020>

Hölzel, M.B., W. Kamermans, B.H.J. Winkelmann, M.H.C. Howlett, C.I. De Zeeuw, and M. Kamermans. 2023. A common cause for nystagmus in different congenital stationary night blindness mouse models. *J. Physiol.* 601:5317–5340. <https://doi.org/10.1113/JP284965>

Jeon, C.J., E. Strettoi, and R.H. Masland. 1998. The major cell populations of the mouse retina. *J. Neurosci.* 18:8936–8946. <https://doi.org/10.1523/JNEUROSCI.18-21-08936.1998>

Jiménez, A.J., J.M. García-Fernández, B. González, and R.G. Foster. 1996. The spatio-temporal pattern of photoreceptor degeneration in the aged rd/rd mouse retina. *Cell Tissue Res.* 284:193–202. <https://doi.org/10.1007/S004410050579>

Kaneko, A., and M. Tachibana. 1985. A voltage-clamp analysis of membrane currents in solitary bipolar cells dissociated from *Carassius auratus*. *J. Physiol.* 358:131–152. <https://doi.org/10.1113/jphysiol.1985.sp015544>

Koike, C., T. Numata, H. Ueda, Y. Mori, and T. Furukawa. 2010. TRPM1: A vertebrate TRP channel responsible for retinal bipolar function. *Cell Calcium.* 48:95–101. <https://doi.org/10.1016/J.CECA.2010.08.004>

Koike, C., T. Obara, Y. Uriu, T. Numata, R. Sanuki, K. Miyata, T. Koyas, S. Ueno, K. Funabiki, A. Tani, et al. 2009. TRPM1 is a component of the retinal ON bipolar cell transduction channel in the mGluR6 cascade. *Proc. Natl. Acad. Sci. USA.* 107:332–337. <https://doi.org/10.1073/PNAS.0912730107>

Kozuka, T., T. Chaya, F. Tamalu, M. Shimada, K. Fujimaki-Aoba, R. Kuwahara, S.I. Watanabe, and T. Furukawa. 2017. The TRPM1 channel is required for development of the rod ON bipolar cell–AII amacrine cell pathway in the retinal circuit. *J. Neurosci.* 37:9889–9900. <https://doi.org/10.1523/JNEUROSCI.0824-17.2017>

Križaj, D., W. Huang, T. Furukawa, C. Punzo, and W. Xing. 2010. Plasticity of TRPM1 expression and localization in the wild type and degenerating mouse retina. *Vis. Res.* 50:2460–2465. <https://doi.org/10.1016/J.VISRES.2010.08.034>

Lagali, P.S., D. Balya, G.B. Awatramani, T.A. Münch, D.S. Kim, V. Busskamp, C.J. Cepko, and B. Roska. 2008. Light-activated channels targeted to ON bipolar cells restore visual function in retinal degeneration. *Nat. Neurosci.* 11:667–675. <https://doi.org/10.1038/NN.2117>

Li, X., M. Sedlacek, A. Nath, K.P. Szatkowski, W.N. Grimes, and J.S. Diamond. 2024. A metabotropic glutamate receptor agonist enhances visual signal fidelity in a mouse model of retinitis pigmentosa. *bioRxiv.* <https://doi.org/10.1101/2024.04.30.591881> (Preprint posted April 30, 2024).

Ly, K., T. Guo, D. Tsai, M. Muralidharan, M.N. Shivedasani, N.H. Lovell, and S. Dokos. 2022. Simulating the impact of photoreceptor loss and inner retinal network changes on electrical activity of the retina. *J. Neural Eng.* 19. <https://doi.org/10.1088/1741-2552/ACAA21>

Maddox, J.W., K.L. Randall, R.P. Yadav, B. Williams, J. Hagen, P.J. Derr, V. Kerov, L. Della Santina, S.A. Baker, N. Artemyev, et al. 2020. A dual role for Cav1.4 Ca^{2+} channels in the molecular and structural organization of the rod photoreceptor synapse. *Elife.* 9:e62184. <https://doi.org/10.7554/ELIFE.62184>

Margolis, D.J., and P.B. Detwiler. 2007. Different mechanisms generate maintained activity in ON and OFF retinal ganglion cells. *J. Neurosci.* 27: 5994–6005. <https://doi.org/10.1523/JNEUROSCI.0130-07.2007>

Margolis, D.J., A.J. Gartland, J.H. Singer, and P.B. Detwiler. 2014. Network oscillations drive correlated spiking of ON and OFF ganglion cells in the rd1 Mouse model of retinal degeneration. *PLoS One.* 9:e86253. <https://doi.org/10.1371/JOURNAL.PONE.0086253>

Margolis, D.J., G. Newkirk, T. Euler, and P.B. Detwiler. 2008. Functional stability of retinal ganglion cells after degeneration-induced changes in synaptic input. *J. Neurosci.* 28:6526–6536. <https://doi.org/10.1523/JNEUROSCI.1533-08.2008>

Masu, M., H. Iwakabe, Y. Tagawa, T. Miyoshi, M. Yamashita, Y. Fukuda, H. Sasaki, K. Hiroi, Y. Nakamura, R. Shigemoto, et al. 1995. Specific deficit of the ON response in visual transmission by targeted disruption of the mGluR6 gene. *Cell.* 80:757–765. [https://doi.org/10.1016/0092-8674\(95\)90354-2](https://doi.org/10.1016/0092-8674(95)90354-2)

Menzler, J., and G. Zeck. 2011. Network oscillations in rod-degenerated mouse retinas. *J. Neurosci.* 31:2280–2291. <https://doi.org/10.1523/JNEUROSCI.4238-10.2011>

Morgans, C.W., J. Zhang, B.G. Jeffrey, S.M. Nelson, N.S. Burke, R.M. Duvoisin, and R.L. Brown. 2009. TRPM1 is required for the depolarizing light response in retinal ON-bipolar cells. *Proc. Natl. Acad. Sci. USA.* 106: 19174–19178. <https://doi.org/10.1073/PNAS.0908711106>

Müller, F., A. Scholten, E. Ivanova, S. Haverkamp, E. Kremmer, and U.B. Kaupp. 2003. HCN channels are expressed differentially in retinal bipolar cells and concentrated at synaptic terminals. *Eur. J. Neurosci.* 17: 2084–2096. <https://doi.org/10.1046/J.1460-9568.2003.02634.X>

Münch, T.A., R.A. Da Silveira, S. Siegert, T.J. Viney, G.B. Awatramani, and B. Roska. 2009. Approach sensitivity in the retina processed by a multi-functional neural circuit. *Nat. Neurosci.* 12:1308–1316. <https://doi.org/10.1038/nn.2389>

Murphy, G.J., and F. Rieke. 2006. Network variability limits stimulus-evoked spike timing precision in retinal ganglion cells. *Neuron.* 52:511–524. <https://doi.org/10.1016/j.neuron.2006.09.014>

Murphy, G.J., and F. Rieke. 2008. Signals and noise in an inhibitory interneuron diverge to control activity in nearby retinal ganglion cells. *Nat. Neurosci.* 11:318–326. <https://doi.org/10.1038/NN2045>

Nakamura, M., R. Sanuki, T.R. Yasuma, A. Onishi, K.M. Nishiguchi, C. Koike, M. Kadowaki, M. Kondo, Y. Miyake, and T. Furukawa. 2010. TRPM1 mutations are associated with the complete form of congenital stationary night blindness. *Mol. Vis.* 16:425–437.

Neuillé, M., C.W. Morgans, Y. Cao, E. Orhan, C. Michiels, J.A. Sahel, I. Audo, R.M. Duvoisin, K.A. Martemyanov, and C. Zeitz. 2015. LRIT3 is essential

to localize TRPM1 to the dendritic tips of depolarizing bipolar cells and may play a role in cone synapse formation. *Eur. J. Neurosci.* 42:1966–1975. <https://doi.org/10.1111/EJN.12959>

Ou, J., C. Vijayasarathy, L. Ziccardi, S. Chen, Y. Zeng, D. Marangoni, J.G. Pope, R.A. Bush, Z. Wu, W. Li, and P.A. Sieving. 2015. Synaptic pathology and therapeutic repair in adult retinoschisis mouse by AAV-RS1 transfer. *J. Clin. Invest.* 125:2891–2903. <https://doi.org/10.1172/JCI81380>

Pan, Z.H. 2000. Differential expression of high- and two types of low-voltage-activated calcium currents in rod and cone bipolar cells of the rat retina. *J. Neurophysiol.* 83:513–527. <https://doi.org/10.1152/JN.2000.83.1.513>

Pearring, J.N., P. Bojang, Y. Shen, C. Koike, T. Furukawa, S. Nawy, and R.G. Gregg. 2011. A role for nyctalopin, a small leucine-rich repeat protein, in localizing the TRP melastatin 1 channel to retinal depolarizing bipolar cell dendrites. *J. Neurosci.* 31:10060–10066. <https://doi.org/10.1523/JNEUROSCI.1014-11.2011>

Poria, D., and N.K. Dhingra. 2015. Spontaneous oscillatory activity in rd1 mouse retina is transferred from on pathway to off pathway via glycinergic synapse. *J. Neurophysiol.* 113:420–425. <https://doi.org/10.1152/JN.00702.2014>

Rentería, R.C., N. Tian, J. Cang, S. Nakanishi, M.P. Stryker, and D.R. Copenhagen. 2006. Intrinsic ON responses of the retinal OFF pathway are suppressed by the ON pathway. *J. Neurosci.* 26:11857–11869. <https://doi.org/10.1523/JNEUROSCI.1718-06.2006>

Schröder, C., J. Oesterle, P. Berens, T. Yoshimatsu, and T. Baden. 2021. Distinct synaptic transfer functions in same-type photoreceptors. *Elife.* 10: e67851. <https://doi.org/10.7554/elife.67851>

Snellman, J., D. Zenisek, and S. Nawy. 2009. Switching between transient and sustained signalling at the rod bipolar-AII amacrine cell synapse of the mouse retina. *J. Physiol.* 587:2443–2455. <https://doi.org/10.1113/JPHYSIOL.2008.165241>

Stasheff, S.F. 2008. Emergence of sustained spontaneous hyperactivity and temporary preservation of OFF responses in ganglion cells of the retinal degeneration (rd1) mouse. *J. Neurophysiol.* 99:1408–1421. <https://doi.org/10.1152/JN.00144.2007>

Strettoi, E., and V. Pignatelli. 2000. Modifications of retinal neurons in a mouse model of retinitis pigmentosa. *Proc. Natl. Acad. Sci. USA.* 97: 11020–11025. <https://doi.org/10.1073/PNAS.190291097>

Strettoi, E., V. Pignatelli, C. Rossi, V. Porciatti, and B. Falsini. 2003. Remodeling of second-order neurons in the retina of rd/rd mutant mice. *Vis. Res.* 43:867–877. [https://doi.org/10.1016/S0042-6989\(02\)00594-1](https://doi.org/10.1016/S0042-6989(02)00594-1)

Strettoi, E., V. Porciatti, B. Falsini, V. Pignatelli, and C. Rossi. 2002. Morphological and functional abnormalities in the inner retina of the rd/rd mouse. *J. Neurosci.* 22:5492–5504. <https://doi.org/10.1523/JNEUROSCI.22-13-05492.2002>

Takeuchi, H., S. Horie, S. Moritoh, H. Matsushima, T. Hori, Y. Kimori, K. Kitano, Y. Tsubo, M. Tachibana, and C. Koike. 2018. Different activity patterns in retinal ganglion cells of TRPM1 and mGluR6 knockout mice. *Biomed. Res. Int.* 2018:2963232. <https://doi.org/10.1155/2018/2963232>

Telias, M., B. Denlinger, Z. Helft, C. Thornton, B. Beckwith-Cohen, and R.H. Kramer. 2019. Retinoic acid induces hyperactivity, and blocking its receptor unmasks light responses and augments vision in retinal degeneration. *Neuron.* 102:574–586.e5. <https://doi.org/10.1016/J.NEURON.2019.02.015>

Telias, M., K.K. Sit, D. Frozenfar, B. Smith, A. Misra, M.J. Goard, and R.H. Kramer. 2022. Retinoic acid inhibitors mitigate vision loss in a mouse model of retinal degeneration. *Sci. Adv.* 8:4643. <https://doi.org/10.1126/SCIADV.ABM4643>

Toychiev, A.H., E. Ivanova, C.W. Yee, and B.T. Sagdullaev. 2013. Block of gap junctions eliminates aberrant activity and restores light responses during retinal degeneration. *J. Neurosci.* 33:13972–13977. <https://doi.org/10.1523/JNEUROSCI.2399-13.2013>

Trenholm, S., J. Borowska, J. Zhang, A. Hoggarth, K. Johnson, S. Barnes, T.J. Lewis, and G.B. Awantramani. 2012. Intrinsic oscillatory activity arising within the electrically coupled AII amacrine-ON cone bipolar cell network is driven by voltage-gated Na⁺ channels. *J. Physiol.* 590:2501–2517. <https://doi.org/10.1113/JPHYSIOL.2011.225060>

Tsodyks, M.V., and H. Markram. 1997. The neural code between neocortical pyramidal neurons depends on neurotransmitter release probability. *Proc. Natl. Acad. Sci. USA.* 94:719–723. <https://doi.org/10.1073/PNAS.94.2.719>

Tsukamoto, Y., K. Morigawa, M. Ueda, and P. Sterling. 2001. Microcircuits for night vision in mouse retina. *J. Neurosci.* 21:8616–8623. <https://doi.org/10.1523/JNEUROSCI.21-21-08616.2001>

Tsukamoto, Y., and N. Omi. 2013. Functional allocation of synaptic contacts in microcircuits from rods via rod bipolar to AII amacrine cells in the mouse retina. *J. Comp. Neurol.* 521:3541–3555. <https://doi.org/10.1002/CNE.23370>

Tsukamoto, Y., and N. Omi. 2017. Classification of mouse retinal bipolar cells: Type-specific connectivity with special reference to rod-driven AII amacrine pathways. *Front. Neuroanat.* 11:92. <https://doi.org/10.3389/fnana.2017.00092>

Ueno, A., K. Sakuta, H. Ono, A. Hashio, H. Tokumoto, M. Watanabe, T. Nishimoto, T. Konishi, Y. Emori, S. Mizuno, et al. 2025. Afadin-deficient retinas exhibit severe neuronal lamination defects but preserve visual functions. *bioRxiv.* <https://doi.org/10.1101/2024.12.24.630271> (Preprint posted September 12, 2025).

Usui, S., A. Ishihara, Y. Kamiyama, and H. Ishii. 1996. Ionic current model of bipolar cells in the lower vertebrate retina. *Vis. Res.* 36:4069–4076. [https://doi.org/10.1016/S0042-6989\(96\)00179-4](https://doi.org/10.1016/S0042-6989(96)00179-4)

Veruki, M.L., and E. Hartveit. 2002. AII (rod) amacrine cells form a network of electrically coupled interneurons in the mammalian retina. *Neuron.* 33:935–946. [https://doi.org/10.1016/S0896-6273\(02\)00609-8](https://doi.org/10.1016/S0896-6273(02)00609-8)

Völgyi, B., S. Chheda, and S.A. Bloomfield. 2009. Tracer coupling patterns of the ganglion cell subtypes in the mouse retina. *J. Comp. Neurol.* 512: 664–687. <https://doi.org/10.1002/CNE.21912>

Winkelmann, B.H.J., M.H.C. Howlett, M.B. Hölzel, C. Joling, K.H. Fransen, G. Pangeni, S. Kamermans, H. Sakuta, M. Noda, H.J. Simonsz, et al. 2019. Nystagmus in patients with congenital stationary night blindness (CSNB) originates from synchronously firing retinal ganglion cells. *PLoS Biol.* 17:e3000174. <https://doi.org/10.1371/JOURNAL.PBIO.3000174>

Xu, Y., A. Dhingra, M.E. Fina, C. Koike, T. Furukawa, and N. Vardi. 2012. mGluR6 deletion renders the TRPM1 channel in retina inactive. *J. Neurophysiol.* 107:948–957. <https://doi.org/10.1152/JN.00933.2011>

Yee, C.W., A.H. Toychiev, and B.T. Sagdullaev. 2012. Network deficiency exacerbates impairment in a mouse model of retinal degeneration. *Front. Syst. Neurosci.* 6:8. <https://doi.org/10.3389/FNSYS.2012.00008>

Zeitz, C., A.G. Robson, and I. Audi. 2015. Congenital stationary night blindness: An analysis and update of genotype-phenotype correlations and pathogenic mechanisms. *Prog. Retin. Eye Res.* 45:58–110. <https://doi.org/10.1016/J.PRETEYERES.2014.09.001>

Zhang, G., J.B. Liu, H.L. Yuan, S.Y. Chen, J.H. Singer, and J.B. Ke. 2022. Multiple calcium channel types with unique expression patterns mediate retinal signaling at bipolar cell ribbon synapses. *J. Neurosci.* 42: 6487–6505. <https://doi.org/10.1523/JNEUROSCI.0183-22.2022>

Supplemental material

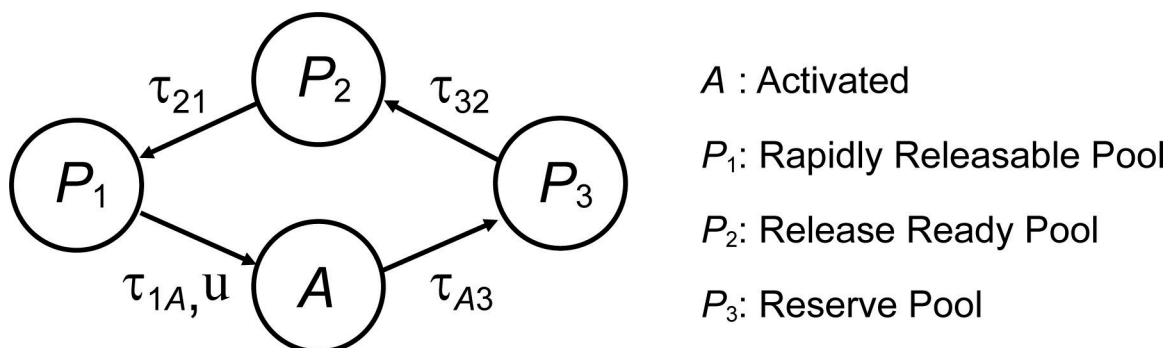


Figure S1. 4-state ribbon synapse model.

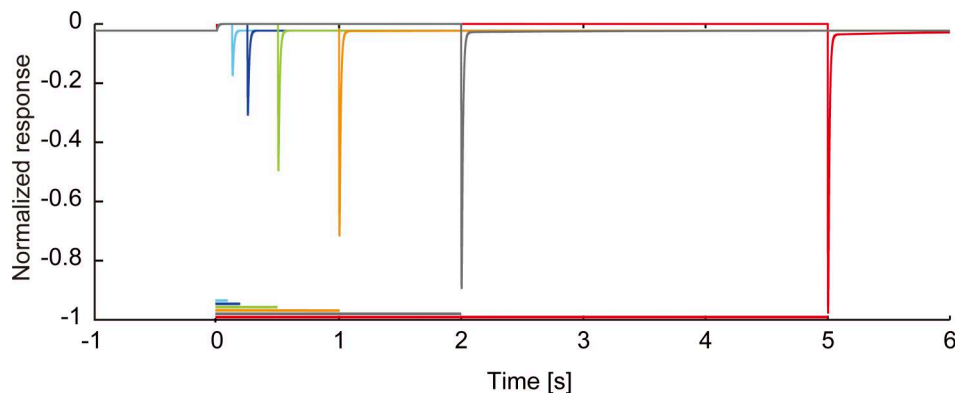


Figure S2. Response recovery of the ribbon synapse model. The magnitudes of the responses following the inactivating voltage step depend on the duration of inactivation. The durations (colored horizontal bars) are 100 [ms] (cyan), 200 [ms] (blue), 500 [ms] (green), 1,000 [ms] (orange), 2,000 [ms] (gray), and 5,000 [ms] (red), respectively.

Provided online are Table S1 and Table S2. Table S1 shows parameter values of synapse models. Table S2 shows connectivity between cells and synaptic conductance.

Modeling part

To investigate the mechanism underlying oscillatory activity observed in *Trpm1* KO and *rd1* mouse retinas, we constructed a computational model of the inner retinal circuit. The model consisted of model neurons (RBCs, ON CBCs, OFF CBCs, AII ACs, ON retinal ganglion cells [ON RGCs], and OFF RGCs) and model synapses (chemical and electrical synapses).

Methods

Models of neurons and synapses

For the three neuronal types, neuron models previously proposed were used. While the BC model was simplified from its original multicompartmental model (Usui et al., 1996) to a single-compartmental model, the other neuronal models were used in their original form (Fohlmeister et al., 2010; Choi et al., 2014). Each neuronal model is conductance-based and incorporates the characteristic electrophysiological properties of the respective cells.

These neuronal models are connected by electrical or chemical synapses. Gap junctions were implemented between ON CBCs and AII ACs, between AII ACs, and between OFF RGCs. ON CBCs were arranged on a triangular lattice and connected with adjacent ones (i.e., six cells) by gap junctions. Gap junctions between OFF CBCs were similarly connected. Ribbon synapses were used for

connections from ON CBCs to ON RGCs, from OFF CBCs to OFF RGCs, and from RBCs to AII ACs. Ribbon synapses possess a specialized structure that enables rapid signal transmission and are considered essential for efficient retinal signaling. The dynamics of neurotransmitter action at these synapses were modeled using transitions between four states, as illustrated in Fig. S1. The state variables (A , P_1 , P_2 , and P_3) represent the ratios of each state, satisfying $A + P_1 + P_2 + P_3 = 1$. The corresponding equations are as follows:

$$\frac{dP_3}{dt} = \frac{A}{\tau_{A3}} - \frac{P_3(P_{2,max} - P_2)}{\tau_{32}} \quad (S1)$$

$$\frac{dP_2}{dt} = \frac{P_3(P_{2,max} - P_2)}{\tau_{32}} - \frac{P_2(P_{1,max} - P_1)}{\tau_{21}} \quad (S2)$$

$$\frac{dP_1}{dt} = \frac{P_2(P_{1,max} - P_1)}{\tau_{21}} - \frac{uP_1}{\tau_{1A}} \quad (S3)$$

$$\frac{dA}{dt} = \frac{uP_1}{\tau_{1A}} - \frac{A}{\tau_{A3}} \quad (S4)$$

τ_{1A} , τ_{A3} , τ_{32} , and τ_{21} are the time constants for the respective state transitions. $P_{1,max}$ and $P_{2,max}$ represent the relative maximum capacities of states P_1 and P_2 , respectively. The parameter values were determined according to the experimental data (Grabner et al., 2016) (Table S1). The presynaptic action described in Eqs. S1, S2, S3, and S4 is basically the same as the model proposed by Schröder et al. (2021). In addition to this presynaptic mechanism, the dynamics of postsynaptic receptor activation, namely, the open probability of the gate variable w , is described by the following equation:

$$\frac{dw}{dt} = \alpha up_1 - \beta w, \quad (S5)$$

where u is the variable that represents release probability of presynaptic neurotransmitter, which is determined by the activation function of the presynaptic membrane potential,

$$u = \frac{1}{2} \left[1 + \tanh \left(\frac{V_{pre} - V_{th}}{V_{slp}} \right) \right], \quad (S6)$$

where V_{pre} is the presynaptic membrane potential, and V_{th} and V_{slp} are the threshold and slope (constants) of the sigmoidal activation function, respectively. This activation function is assumed to reflect the activation function of high-voltage-activated calcium channels (de la Villa et al., 1998). As shown in Fig. S2, this ribbon synapse model could reproduce the kinetics of the cone-OFF CBC synapse, responses to presynaptic voltage step (Grabner et al., 2016). The glycinergic synapses from AII ACs to OFF CBCs and OFF RGCs are conventional (not ribbon) synapses. The kinetics of this synapse type is modeled using a modified version of the depressing synapse model (Tsodyks and Markram, 1997), adapted for graded presynaptic potentials,

$$\frac{dE}{dt} = -\frac{E}{\tau_E} + UsR \quad (S7)$$

$$\frac{dR}{dt} = \frac{1 - R - E}{\tau_R} - UsR \quad (S8)$$

$$s = \frac{1}{2} \left[1 + \tanh \left(\frac{V_{pre} - V_{th}}{V_{slp}} \right) \right] \quad (S9)$$

E and R represent the effective and recovered states of neurotransmitter, respectively. E represents the open-state ratio of postsynaptic channels. U , τ_E , and τ_R are constants representing the release probability, the time constant of inactivation, and the time constant of recovery, respectively. The variable s corresponds to u in the ribbon synapse model described above.

Connectivity between cells

The proposed retinal circuit model consists of 126 RBCs, 28 ON CBCs, 64 OFF CBCs, 14 AII ACs, 1 ON RGC, and 5 OFF RGCs. These cell numbers were determined as the minimum required to satisfy the connectivity between cells. The connection patterns and the number of connections for each cell type were determined based on previous studies (Tsukamoto et al., 2001; Margolis and Detwiler, 2007; Völgyl et al., 2009; Arai et al., 2010; Arman and Sampath, 2012; Tsukamoto and Omi, 2017) as summarized in Table S2.

Photoreceptor cells were not included in the model. Instead, the presence or absence of light stimuli was reproduced by applying nonzero or zero input currents, respectively, to the BC models.

Simulation conditions

The simulation was performed according to the following procedure. (1) Constructing a normal retinal neural circuit model: based on experimental results obtained from normal retinas, we constructed a model that reproduces normal responses to light stimuli, such as ON and OFF responses (Dunn et al., 2006; Margolis and Detwiler, 2007; Arman and Sampath, 2012). (2) Applying known

pathological conditions: the pathological conditions identified in previous research (Takeuchi et al., 2018) were applied to the model constructed in step 1. These conditions include a reduction in transient inputs from photoreceptor cells to BCs and a reduction in inputs from RBC to AII ACs. However, additional unidentified conditions might also be necessary to fully reproduce the abnormal activity observed in the pathological retinas. (3) Exploring the conditions for RGC oscillations: using the model constructed in step 2, we explored the conditions under which RGCs exhibit abnormal periodic spontaneous firing. One candidate is the threshold of the activation function for neurotransmitter release (V_{th} in Eq. S9). This is because the membrane potential of ON CBCs is supposed to be hyperpolarized under the pathological conditions (*Trpm1* KO and *rdl*). To enable synaptic activation of ON RGCs even under such conditions, neurotransmitter release should be maintained. Lowering the threshold, which could be attributed to the involvement of T-type calcium channels (Pan, 2000), enables such maintenance.